

# Automated Detection of Double Nuclei Galaxies using GOTHIC and the Discovery of a Large Sample of Dual AGN

Anwesh Bhattacharya<sup>1</sup>, Nehal C. P.<sup>2</sup>, Mousumi Das<sup>3</sup>, Abhishek Paswan<sup>3,4</sup>, Snehanshu Saha<sup>5\*</sup>, Françoise Combes<sup>6</sup>

<sup>1</sup>*Dept. of Physics and CSIS, Birla Institute of Technology & Science, Pilani, India*

<sup>2</sup>*Dept. of Physics, Indian Institute of Science Education and Research, Bhopal*

<sup>3</sup>*Indian Institute of Astrophysics, Bangalore*

<sup>4</sup>*Department of Physics, University of Allahabad, India*

<sup>5</sup>*APPCAIR, Dept. of CSIS, Birla Institute of Technology & Science, Goa, and HappyMonk AI, India*

<sup>6</sup>*Observatoire de Paris, LERMA, Collège de France, PSL University, Sorbonne University, CNRS, Paris, France*

Accepted 2023 July 10. Received 2023 July 10; in original form 2022 November 16

## ABSTRACT

We present a novel algorithm to detect double nuclei galaxies (DNG) called GOTHIC (Graph-Boosted iterated Hill Climbing) — that detects whether a given image of a galaxy has two or more closely separated nuclei. Our aim is to test for the presence of dual/multiple active galactic nuclei (AGN) in galaxies that visually represent a DNG. Although galaxy mergers are common, the detection of dual AGN is rare. Their detection is very important as they help us understand the formation of supermassive black hole (SMBH) binaries, SMBH growth and AGN feedback effects in multiple nuclei systems. There is thus a need for an algorithm to do a systematic survey of existing imaging data for the discovery of DNGs and dual AGNs. We have tested GOTHIC on an established sample of DNGs with 100% detection rate and subsequently a blind search of 1 million SDSS DR16 galaxies (with spectroscopic data available) lying in the redshift range of  $z = 0$  to 0.75. From the list of candidate DNGs found, we have detected 159 dual AGNs, of which 2 are triple AGN systems. Our results show that dual AGNs are not common, and triple AGN even rarer. The color (u-r) magnitude plots of the DNGs indicate that star formation is quenched as the nuclei come closer and as the AGN fraction increases. The quenching is especially prominent for dual/triple AGN galaxies that lie in the extreme end of the red sequence.

**Key words:** galaxies : interactions – galaxies : active – galaxies : nuclei – galaxies : evolution – techniques: image processing – methods: numerical

## 1 INTRODUCTION

Galaxy mergers are the main mechanism for the hierarchical growth of galaxies in our universe (White & Rees 1978; Patton et al. 2020). Depending upon the gas content of galaxies, gas rich mergers can lead to substantial amounts of star formation, resulting in starbursts and ultraluminous infrared galaxies (ULIRG hereafter) (Sanders & Mirabel 1996). Dry or gas free mergers of elliptical and S0 galaxies do not result in star formation but lead to the growth of more massive early type galaxies (Thomas et al. 2005). As galaxies merge, the bulges and nuclei of the individual galaxies come closer leading to the formation of dual or even multiple nuclei systems that are often enclosed within a single galaxy envelope (Capelo et al. 2017). In the process, one or more of the supermassive black holes (SMBH hereafter) in the galaxy nuclei may start accreting mass leading to the formation of active galactic nuclei (AGN hereafter) (Shlosman et al. 1990; Peterson 1997). Alternatively, large amounts of gas may fall into the nuclear regions of the merging galaxies triggering nuclear starburst activity (Kim et al. 2021).

Thus, double nuclei galaxies (DNG hereafter) can host AGN pairs, AGN-starburst pairs or individual star forming nuclei in their centers (Rubinur et al. 2019; De Rosa et al. 2019). When two or more AGN are found in a merger remnant and are separated by  $<10$  kpc, it is often termed as a dual AGN (DAGN hereafter) system, although the definition varies in the literature and can include AGN at separations of upto  $\sim 50$  kpc (Koss et al. 2012). Triple AGN systems have also been detected in small groups of merging galaxies (Yadav et al. 2021) which suggests that multiple AGN systems are more common than we think. In fact simulations have shown that minor mergers can lead to many massive black holes (MBHs) that are spatially offset from the central galaxy nucleus; such MBHs are called "wandering black holes", since they do not appear to be in the process of merging with the nuclear SMBH (Bellovary et al. 2010; Ricarte et al. 2021). A few wandering MBHs have been detected (Greene et al. 2021; Reines et al. 2020). If an AGN pair is separated by only a few parsecs or  $<1$  kpc, it is termed as a binary AGN (BAGN). The number of DAGN identified till now is  $<100$  (Rubinur et al. 2018; Stemo et al. 2021) and the number of confirmed binary AGN is  $<10$  (Kharb et al. 2017a; Ciurlo et al. 2023). These numbers are small compared to the total fraction of AGN detected in galaxies at low redshifts. Since galaxy

\* Corresponding author - snehanshu.saha@ieee.org

mergers are common, this suggests that there is a large population of dual/multiple AGN systems that have not yet been detected.

Most of the early detections of DAGN in the literature were serendipitous, and were discovered during galaxy surveys of emission line galaxies and merger remnants (Komossa et al. 2003) or radio observations of compact sources (De Rosa et al. 2019). Later studies used double peaked AGN emission line galaxies (DPAGN hereafter) to search for DAGN (Zhou et al. 2004; Rubinur et al. 2019; Maschmann et al. 2020). However, DPAGN can also be due to AGN outflows or rotating disks (Kharb et al. 2017b). Recent studies have shown that one of the best ways to detect DAGN is by using a parent sample of dual nuclei galaxies and then identifying the nature of their nuclei using multi-wavelength observations (De Rosa et al. 2019; Scialpi et al. 2023; Koss et al. 2023a). However, the latest surveys of galaxy pairs are either too small or the nuclei separations are too large to be defined as dual nuclei systems (Patton et al. 2016).

There are several reasons why we need to find more dual or multiple AGN systems. One of the most important reasons is that they represent the first stage in the formation of SMBHs pairs. At distances of several Mpc beyond the local universe, the only way to detect SMBHs is via the radiation emitted from AGN activity. Although the gravitational radiation from SMBH pairs is emitted only when they are separated by less than a parsec, a large sample of DAGN will help us understand how they form and evolve. So revealing the frequency and nature of SMBH pairs is the first step in understanding the low frequency (nano Hz) gravitational waves radiated by inspiralling SMBHs (Aggarwal et al. 2019; Goulding et al. 2019; Shannon et al. 2015). Secondly, although dual AGN/multiple AGN are rare, it has been shown that galaxy mergers are important triggers of AGN activity and the formation of DAGN, both of which can lead to nuclear star formation and SMBH growth. Simulations have suggested that merger-triggered AGN may dominate SMBH growth (Hopkins et al. 2014). Finally, SMBH pairs or clusters will affect the AGN feedback and stellar winds/outflows associated with galaxy mergers, which can result in the growth of the circumgalactic medium (CGM hereafter) around galaxies (Fielding et al. 2020; Davies et al. 2020). Multiple AGN can give rise to stronger winds and outflows, producing additional feedback effects as observed in nearby DAGN (Mazzarella et al. 2012; Rubinur et al. 2020). Hence, large samples of DAGN are essential for fully understanding the role of mergers in SMBH growth and galaxy evolution.

In this paper we present an automated search for dual/multiple nuclei in merging and interacting galaxies, using an algorithm called `GOTHIC` that detects such systems using optical images. We applied `GOTHIC` to SDSS images and derived a large sample of double and multiple nuclei in closely interacting galaxies and merger remnants. Our broad goal is to create a large sample of dual or multiple nuclei from which we can detect DAGN (or even multiple AGN systems). In Section 2 we first review previous studies that search for galaxy pairs and then build the case for the need of a large catalog of DNGs. We also discuss the trial sample that was used as a benchmark for developing the algorithm. In Section 3, we describe the design of the algorithm. The algorithm has been carefully designed such that it achieves a 100% detection rate on the trial sample, whilst keeping the false positive rate reasonably low on previously unseen samples.

We subsequently performed a blind search by applying the algorithm on a large sample of 1 million galaxies and detected  $\approx 100,000$  candidate DNGs. We filtered these candidates and manually analyzed a smaller subset of them in Section 4 and Section 5. We then present the DNGs in a catalogue and discuss their properties. We have separated out the dual and multiple AGN in the sample and discussed the nature of the host galaxies. Finally, we conclude with

a discussion of the impact of our study on understanding DAGN and galaxy mergers in Section 6 and Section 7.

## 2 WHY AUTOMATE THE SEARCH OF DOUBLE NUCLEI GALAXIES?

### 2.1 Previous Studies and our Motivation

Large samples of galaxy pairs have been previously derived in the literature from imaging or spectroscopic surveys, by selecting the nearest neighbor galaxies. This was usually done by constructing radial bins around galaxies and selecting neighboring galaxies that lie within specific radii from the target galaxy (e.g.  $R < 2$  Mpc) (Bustamante et al. 2020). Alternatively, differences in systemic velocities between a target galaxy and its neighbors have been used to derive the closest neighbors (Maschmann et al. 2020). Although this method did select galaxy pairs, it was mainly aimed at detecting the tidal features in interacting galaxies (Ellison et al. 2010) and the effect of galaxy interactions on star formation (Barton et al. 2000; Patton & Atfield 2008). Most of the galaxy pairs that were detected in these surveys were separated by several megaparsec (Mpc) distances, and hence these samples basically represent galaxies interacting at a distance but not actually merging. Many of these surveys also have constraints on the mass ratios of the two galaxies and contain distant pairs and not close galaxy pairs (Bustamante et al. 2020). These methods are thus biased towards detecting galaxies interacting at a distance rather than merger remnants that contain two or more nuclei encased in a single envelope that represent closely interacting galaxies.

There have recently been several studies of galaxy pairs in cosmological simulations. These studies use hydrodynamical simulations to emulate galaxy mergers which are then used to build mock samples upon which an image-classification scheme is developed. However, some studies suggest that mock images may result in poor performance in merger classifications (Bottrell et al. 2019). Others have performed convolutional neural network (CNN) training on processed isolated galaxy images (e.g. IllustrisTNG) for the task of automated merger classification (Bickley et al. 2021; Nelson et al. 2019). They obtain a sample with a purity of only 6% due to the intrinsic rarity of galaxy mergers. Thus, there is clearly some difficulty in building a clean sample of galaxy mergers using simulations (Nevin et al. 2019). Studies have also compared the efficiency of using stellar kinematics versus visual images and found that visual identification is better (Bottrell et al. 2021). This is clearly demonstrated in (Blumenthal et al. 2019) where samples of *Visually Identified Pairs* (VIP) are presented using simulated images from IllustrisTNG.

Thus there is a need for an algorithm and pipeline that can sift through large optical or near-infrared (NIR) imaging surveys of real galaxies and extract double/multiple galaxy nuclei efficiently with no bias with respect to spatial separations, galaxy mass ratios or redshift ranges of the galaxies. Such a method will be computationally more efficient compared to counting nearest neighbors in radial bins. It is with this aim in mind that we have developed an algorithm that can detect dual nuclei systems at kiloparsec (kpc) scale separations from an optical survey and identify a pool of dual nuclei systems that can be used to study galaxy mergers and detect candidate dual/multiple AGN systems. In the following section we discuss the trial sample of dual nuclei that we have used in our study.

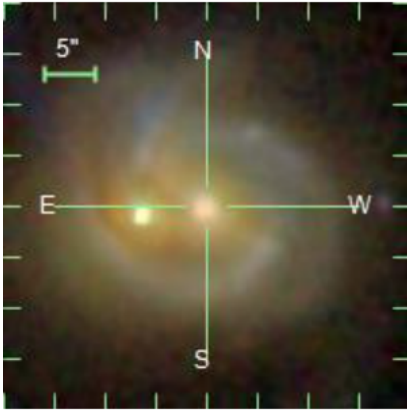


**Figure 1.** Color composite SDSS image of MRK 739 showing clearly the two nuclei.

## 2.2 The Trial Sample

Since DNGs are a rare type of galactic object, it is essential to have a sample of established DNGs which can be used as a benchmark to check the performance of our algorithm. The Gimeno Catalog (Gimeno et al. 2004) presents a compiled sample of 107 DNGs from previously existing catalogs. They have also used ESO plates to catalogue the sources. However, we found that only 47 galaxies out of the 107 had valid entries in SDSS DR16. Thus, we used these 47 galaxies as the trial sample.

MRK 739 (Figure 1) is a prototypical example of the type of galaxy we are interested in detecting. It was first studied in detail by Koss et al. (2011) where it was confirmed to host a DAGN. It was more recently studied by Tubin et al. (2021) who identified the western and eastern nuclei to be on their ongoing first passage. The construction of our algorithm is targeted towards finding galaxies that resemble the visual features of MRK 739 *i.e.*, there should be two distinct bulges.

The GC catalog was subsequently used by Mezcua et al. (2014) in which they selectively studied DNGs that were available in SDSS DR8. The study focuses on classifying the DNG sources as major/minor mergers and to find evidence for AGN activity in the DNGs. This is because DNGs are a strong candidate for DAGN systems and detecting them accurately can help in building a catalog of DAGNs. In fact, there are numerous studies showing that visual DNG systems turn out to be hosts for DAGNs (Rubinur et al. 2020; Koss et al. 2012; Komossa et al. 2003; Williams et al. 2021; Koss et al. 2023b).

## 3 DESCRIPTION OF THE PROCEDURE

To determine whether a galaxy is a DNG we need to first have image cutouts of galaxies from SDSS. Figure 1 is an example of a color composite image of a DNG in the SDSS display in object explorer<sup>1</sup>. It is a  $40'' \times 40''$  square-cutout centred on the coordinates with which the `objID` of the galaxy is associated. A successful algorithm for DNG detection must be able to identify the light envelope of one galaxy or two close galaxies, and detect the presence of two distinct bulges if any. In practice, however, `objID` of galaxies in SDSS do not always faithfully correspond to a galaxy *i.e.*, some IDs correspond

<sup>1</sup> <http://skyserver.sdss.org/dr16/en/tools/explore/summary.aspx>

	Ground Truth		Total
	Double	Single	
<i>GOTHIC</i> 's output			
Double	47 (TP)	7 (FP)	54
Single	0 (FN)	40 (TN)	40
Total	47	47	94

**Table 1.** Confusion Matrix of *GOTHIC*: Double nuclei galaxies represent positives examples, and single nuclei galaxies are negative examples. The standard abbreviations have been used *i.e.*, TP is True Positive, FP is False Positive, TN is True Negative, and FN is False Negative.

to stars, QSOs, or blank patches of sky with no visible object in its vicinity. So the detection procedure must carefully handle mislabelled galaxies. This unreliable nature of the *ground truth* of SDSS labels has been previously documented (Makhija et al. 2019).

In terms of its functionality, the *GOTHIC* algorithm takes as input a  $40'' \times 40''$  square cutout of a galaxy and classifies it as a DNG or a single-nuclei galaxy. In a nutshell, this classification is done by searching for two well-defined peaks of light that are characteristic of DNGs. The algorithm consists of six major components which are briefly summarized below

- (i) **Image Normalization and Smoothing** - The first step of the algorithm is to smooth the input image so that it is amenable to further processing
- (ii) **Edge Detection** - The galaxy of interest occupies a portion of the  $40'' \times 40''$  cutout space. To visually identify the boundaries of the galaxy, we use the Canny edge detector (Canny 1986).
- (iii) **Fitting the Light Profile** - After the galaxy has been located in the cutout, we compute a histogram of the pixel values contained in the galaxy. This histogram is then fit to a Sérsic light profile (Sérsic 1963) to determine the Sérsic index.
- (iv) **Determination of the Search Region** - After determining the exact Sérsic profile, a pixel *cutoff value* is calculated. Only the pixels above this cutoff value are the ones with appreciable light intensity. The search for light peaks occurs in the region above this cutoff value.
- (v) **Iterated Hill Climbing** - This is a formal algorithm for locating peaks of light in the search region determined by the previous step.
- (vi) **Final Classification** - Typically, more than 2 peaks are detected for a given galaxy. This occurs since the cutout images are inherently noisy, even after smoothing. Using all the information determined by all previous steps, we develop a sound rule-based system to judge whether the peaks represent those of a DNG or not.

Detailed descriptions of each of the above 6 steps can be found in Supplementary Section 1.

### 3.1 Testing the performance of *GOTHIC*

Having developed *GOTHIC*, we tested its performance on a test sample that comprises the following

- (i) **Positive sample** - All the 47 galaxies in the trial sample serve as the positive sample.
- (ii) **Negative control sample** - We randomly selected 47 single nucleus galaxies from SDSS DR16. We ensured the size of control sample was equal to the positive sample for fairness.

We found that *GOTHIC* had a 100% detection rate on the positive sample *i.e.*, all DNGs were correctly recognized and there were 0 false negatives. On the other hand, only 7 galaxies from the control sample were incorrectly recognized as DNGs. This represents a

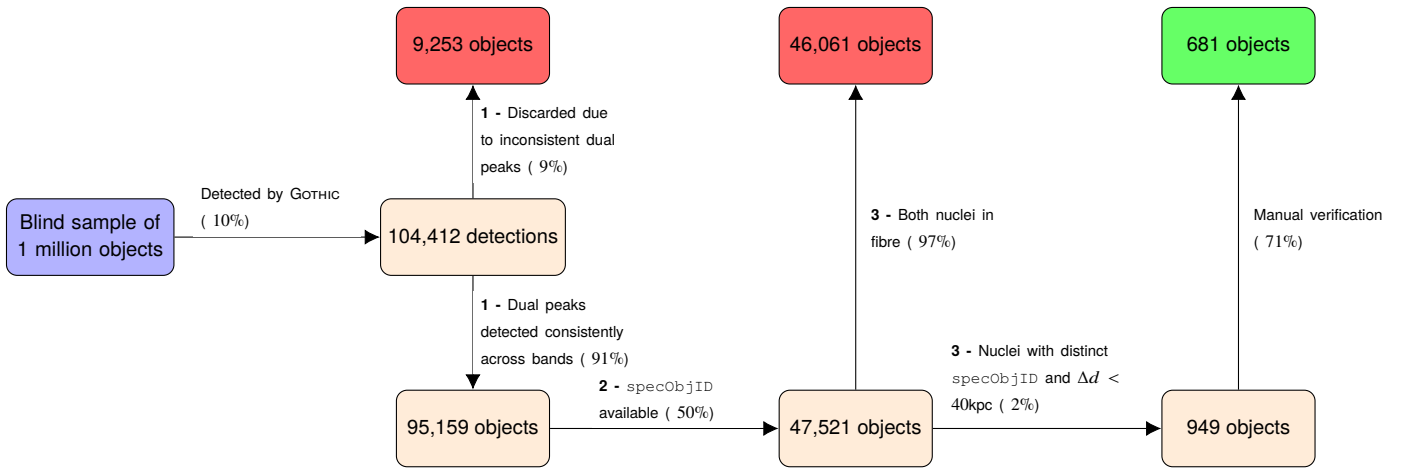


**Figure 2.** Flowchart demonstrating the filtration of the blind sample down to the visually confirmed sample. The bold numbers refer to the filtration steps in Section 4 and the numbers in parenthesis indicate the percentage reduction in the sample size caused by each filtration step

false positive rate of 15%. To visualize the various detections in a concise format, we provide a concise confusion matrix in Table 1. The details of GOTHIC’s performance on the test sample can be found in Supplementary Section 2.

#### 4 APPLYING GOTHIC TO A LARGE BLIND SAMPLE

As stated previously in Section 2, our goal is to prepare a sample of candidate DAGNs. To do so, we first need to identify galaxies that visually resemble DNGs and subsequently analyse their spectra to confirm if it is truly an AGN. Given GOTHIC’s 100% detection rate on the Gimeno Catalog, we can expect that if the image given to it were that of a DAGN, it would recognize it as a DNG with high certainty. Thus, if it is run upon a large sample of randomly chosen galaxies (most of which are bound to be single nucleus galaxies), it will filter out those rare galaxies that resemble DNGs. To that end, we ran GOTHIC on 1 million galaxies chosen uniformly at random from SDSS DR16 that have spectroscopic data available. The galaxies were chosen uniformly at random so that there is no bias towards any physical property (such as redshift or magnitude in any band). We used images in the  $u, g, r, i$  bands and discarded the  $z$  band as we found images in this band to be often noisy. Among the 1 million randomly chosen galaxies, GOTHIC detected 104,412 DNGs which represents an overall hit rate of  $\approx 10\%$ . However, using these raw detections for further analysis is not suitable due to the following reasons

- (i) Extrapolating from GOTHIC’s performance on the trial sample, we can expect false positives in the detections which need to be filtered out.
- (ii) The raw detection sample is too large to be analysed manually.

##### 4.1 Filtration Steps to Obtain a Reduced Sample

Thus we need to filter the raw detections such that — i) Detections that are likely to be false positives are removed. ii) The reduced sample will only contain those detections that are highly likely to be DAGN after manual analysis. Thus we applied the following sequence of conditions to arrive at a smaller sample that could be manually studied (depicted as a flowchart in Figure 2).

**Filtration Step 1** - The pixel coordinates of the detected nuclei need

to be consistent across all the bands in which they are detected in. For example, if a peak is detected at  $(x, y)$  in the  $g$  band and GOTHIC reports a double detection in the  $r$  band, a corresponding peak has to be present in the  $r$  band within the  $3 \times 3$  window centred at  $(x, y)$ . If a given galaxy has a consistent detection of peaks across all bands in which GOTHIC reports a detection, we denote it as a *pure double*. Otherwise, we denote it as an *impure double* and intuitively these galaxies are more likely to be false positives. We found 95,159 pure doubles and used this subset for further filtration. The remaining 9,353 impure doubles were exempt from further study.

**Filtration Step 2** - Although our initial one million sample had spectroscopic data available, it is not necessarily true that the DNG detected by GOTHIC always correspond to the galaxy referenced by its `objID`. GOTHIC is purely an image processing algorithm and is unaware of the mapping between galaxies/peaks and `objIDs`. Thus, we performed a coordinate to `objID` lookup of the DNGs detected by GOTHIC. We found that 47,521 of the 95,159 pure doubles have spectroscopic data available in SDSS (indicated by an existing `specObjID` entry). Spectroscopic information is needed in our final analysis (redshift distribution, for example) and thus this step is necessary.

**Filtration Step 3** - Of this filtered spectroscopic DNG sample, we choose only those DNGs that have distinct `specObjIDs` corresponding to *both* the peaks of the DNGs. So from the 47,521 candidate DNGs, we obtained two groups of sources — i) The first was composed of 46,061 DNG candidates where both nuclei were located within the SDSS fibre which has a diameter  $3''$ . These sources could not be distinguished as two spectroscopic sources and hence discarded. ii) The second group is a sample of 949 DNGs where both nuclei have distinct `specObjIDs` and are very close in redshift ( $z$ ). The cutoff for  $\Delta z$  separation is defined by a distance ( $d$ ) which is taken to be approximately  $\Delta d < 40\text{kpc}$ , for all redshifts. This is the harshest filtration step as it retains only 2% of the previous sample. If SDSS catalogues distinct `specObjIDs` at the location of the peaks, we gain additional confidence that the detection is a true positive.



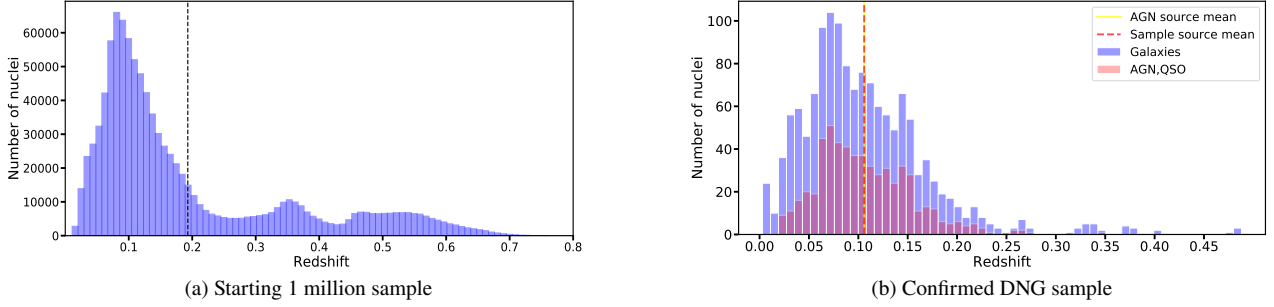


**Figure 3.** Redshift Distributions

**Table 2.** Frequency of each possible combination

combination	count
AGN-AGN	153
AGN-AGN-AGN	2
AGN-AGN-SF-SF	1
AGN-AGN-SF	3
AGN-SF	150
AGN-SF-SF	1
SF-SF	152
SF-SF-SF	2

#### 4.2 Justification for Choosing a Spectroscopic Sample

In our preliminary experiments of deploying `GOTHIC` to an unknown sample of galaxies, we found numerous detections of DNGs most of which turned out to be false positives. Upon manual investigation, these detections were essentially that of large foreground stars with diffraction spikes that dominated the space of the  $40'' \times 40''$  cutout. We provide an example of such an object along with its DR16 link<sup>2</sup>. According to SDSS, this object has its “type” attribute named as “GALAXY” with a valid photometric redshift. Using samples with a valid spectroscopic redshift would automatically eliminate such *contaminants* in the starting blind sample. Moreover, the final outcome of running `GOTHIC` through a blind sample was to obtain a reduced sample which we could study for further insight. With this goal in mind, it was decided that the initial blind sample only contain galaxies with available spectroscopic redshift. Further justifications for choosing a spectroscopic sample have been provided in the Supplementary Section 1.5.1.

## 5 ANALYSIS OF THE REDUCED CANDIDATE SAMPLE

### 5.1 The final sample of galaxy nuclei pairs

We visually checked the sample of 949 nuclei pairs to determine the success rate of `GOTHIC`. We found that 681 were true galaxy nuclei pairs, which gives a success rate of 71%. The false detection were mainly because of the following reasons.

(i) The target galaxy did not have a compact bulge or nucleus and so `GOTHIC` incorrectly classified it as a merger (e.g. objID: [1237663239272923278](https://skyserver.sdss.org/dr16/en/tools/explore/Summary.aspx?id=1237663239272923278))

(ii) The companion galaxy did not have a redshift, even though it was classified as a spectroscopic source (e.g. objID: [1237671124306231474](https://skyserver.sdss.org/dr16/en/tools/explore/Summary.aspx?id=1237671124306231474))

(iii) The system appears to be a merger but the second galaxy does not have a clear nucleus (e.g. objID: [1237658204507340929](https://skyserver.sdss.org/dr16/en/tools/explore/Summary.aspx?id=1237658204507340929)).

### 5.2 The redshift distribution of the initial and final samples

**Figure 3a** shows the redshift distribution of the initial sample of one million galaxies from SDSS DR16. The redshift extends from  $z = 0$  to 0.832 and shows three peaks at approximately  $z = 0.079, 0.353, 0.494$ . The redshift distribution of the confirmed DNG (**Figure 3b**) is however slightly different and is distributed mainly between redshifts of  $z = 0$  to 0.3. It shows only one peak at approximately  $z = 0.073$ , which is close to the first peak of the one million galaxy distribution, but does not have the exact same value. A significant fraction of the 681 sources are classified as DAGN pairs using SDSS and their distribution is overlaid in pink. The DAGN have the same distribution as the nuclei pairs. The mean redshifts of the nuclei pairs and DAGN are very close to each other and are at  $z \approx 0.1$  as shown by the dashed vertical line in **Figure 3b**.

### 5.3 The classification of nuclei pairs using emission line ratios (BPT plot)

As described in the introduction, our aim was to find a sample of DAGN (Rubinur et al. 2020) or multiple AGN (Yadav et al. 2021) systems. To obtain such a sample, the SDSS class of the nuclei was very important. The SDSS classifies nuclei according to the emission lines in the spectra and the commonly used classes are starforming, starburst, AGN and QSO (Jönsson et al. 2020). If an AGN has broad components in the emission lines with doppler widths  $>200 \text{ km s}^{-1}$  it is classified as AGN broadline. The quasars (QSO), which are the most powerful AGN and have very broad emission lines, are identified using spectral templates.

In our sample of 949 nuclei pairs, 681 were visually confirmed to be nuclei pairs. We also found that many of the nuclei pairs in our sample are in small groups. This is not surprising as the clustering of galaxies has been known for decades (Dressler 1984). Using the SDSS class, we found that 11 nuclei pairs were DAGN, and either QSO-QSO or AGN-QSO pairs. The subclass of the nuclei were extracted from SDSS wherever it was available and this gave finally 45 DAGN. But we found that SDSS DR16 had tabulated the class and subclass for relatively few sources and hence this gave us a low number of DAGN which did not seem to be complete.

So for a better classification of the nuclei, we instead used the SDSS tabulated emission line data of the nuclei to plot the Baldwin, Phillips

<sup>2</sup> <https://skyserver.sdss.org/dr16/en/tools/explore/Summary.aspx?id=1237680332175769803>

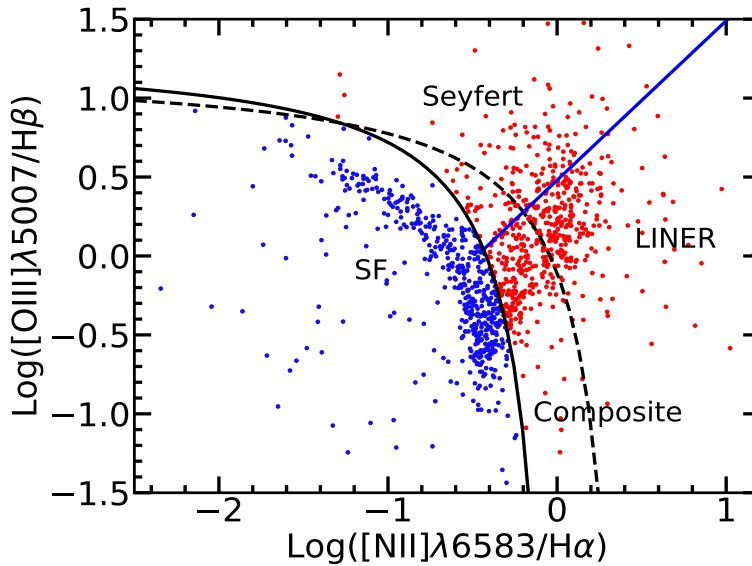


**Figure 4.** The BPT Diagram of the emission line data of 1098 nuclei that lie in pairs or small groups i.e. they are derived from the sample of 681 DNGs. From the position of the nuclei, their nature could be explained with reference to classification curves: The black solid line is the curve fit signifying the lower limit for AGNs (Kauffmann et al. 2003), hence the region below this curve is considered as SF (marked by blue dots). Similarly, the region above this curve is considered as AGN (marked by red dots). The black dashed curve is the upper limit for star burst (Kewley et al. 2006), sources in region between the solid black curve and dashed black curve are considered composite. The solid blue line separated LINER from Seyferts (Fernandes et al. 2010)

The distribution obtained is as follows : SF=517, composite=244, LINER=232 and Seyfert=105

and Terlevich (BPT) diagram of our 681 DNG sources (Baldwin et al. 1981). The BPT classifies nuclei based on the ratio of emission lines such as  $H\alpha$ , [OIII], [SII], [NII]. Out of the total sample of 681 sources we have tried to incorporate the emission line data of all the nuclei for which data was available and obtained line data for 1393 nuclei (Figure 4). The classes of the nuclei are star forming (SF hereafter), composite, LINER and Seyfert. We have taken the solid curve in the Figure 4 as the lower limit for finding an AGN and hence the classes composite, LINER and Seyfert are all considered to be AGN (Kauffmann et al. 2003). Studies have shown that the composite class does host AGN (Juneau et al. 2014).

However, there were some problems in obtaining the exact nature of some nuclei mainly because :

- (i) Out of 1393 nuclei 14 had unavailable line emission data
- (ii) 258 nuclei had either one of the emission line fluxes tabulated as negative or the denominator in the flux ratio was 0.
- (iii) 22 had negative emission line line fluxes but the ratio was positive
- (iv) One source had unusual [OIII] emission line values

So finally we could classify the nature of 1098 nuclei, of which 581 were AGN in nature and 517 were star forming. So the final BPT plot had 1098 nuclei (Figure 4). We examined the nature of the sources in detail and found that 159 sources had at least two of the nuclei classified as AGN, so the number of DAGN detected in our sample is 159 (Table 2). However, it must be noted that this is a lower limit, as the spectral information for several nuclei sources was not available. Of these 159 DAGN, 2 are in clusters of triple AGN lying with groups of 3 to 4 galaxies. Triple AGN are rare and only a few have been detected using X-ray and optical observations (Yadav et al. 2021). One DAGN is in a group of 4 nuclei with the other two being star forming in nature. One DAGN is in a triplet system where the third is a star forming nucleus.

The frequency of the different combinations obtained is given

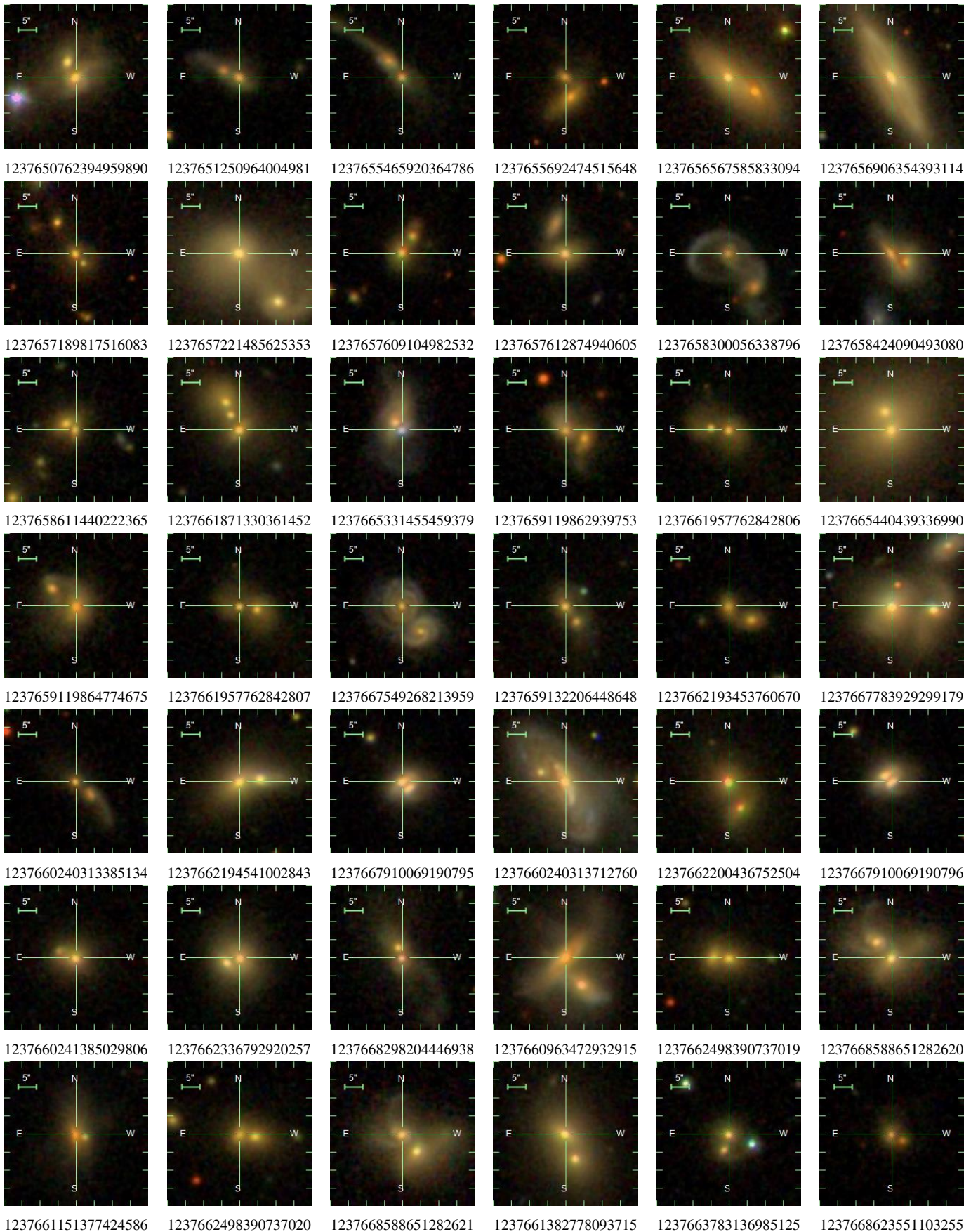
in Table 2. It is clear that the number of AGN-SF and DAGN are comparable. This is surprising as the number of star forming nuclei is generally found to be larger than the number of DAGN in previous studies (e.g. Rubinur et al. (2019)). But our sample is composed of relatively close nuclei pairs, hence this suggests that star formation maybe quenched in galaxies as the nuclei come closer during mergers. Table 2 also shows that the number of composite class nuclei is relatively large. These nuclei have star formation associated with AGN activity and may represent galaxies evolving from starburst dominated galaxies to AGN dominated ones (Yuan et al. 2010). The number of star forming (SF-SF) or AGN-SF pairs is also very large, implying that star formation is an integral part of the interaction process, but may not be the dominant one as the number of SF-SF nuclei and DAGN are comparable.

The full table of the 159 sources is available in Table 3. Also, a panel depicting a subset of the sources (42 of them) are presented in Figure 5.

#### 5.4 The color magnitude plot of the galaxy nuclei pairs and comparison with the general population of SDSS galaxies

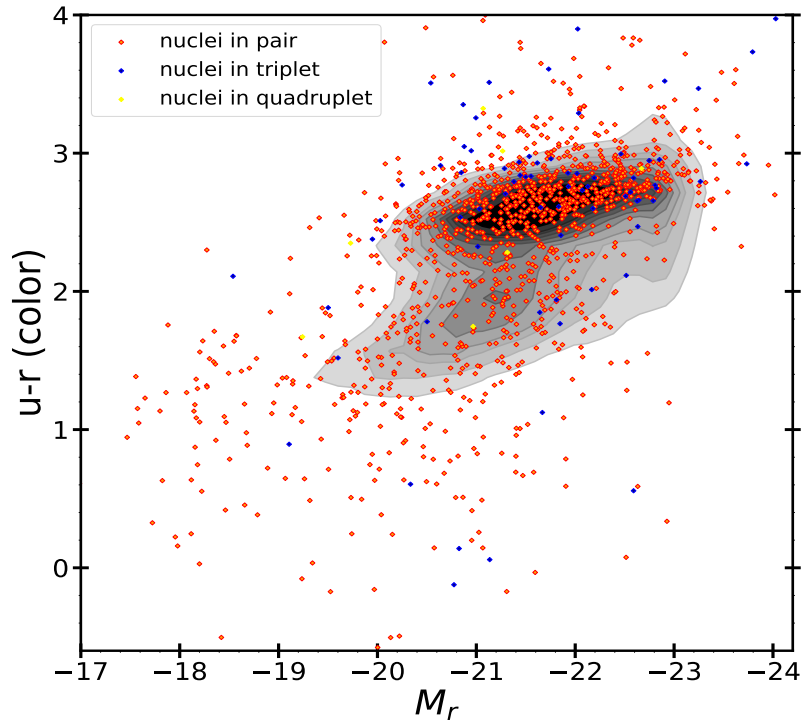
The color magnitude diagram (CMD) of galaxies is usually a plot of the color of galaxies (e.g.  $u - r$  magnitudes) against their absolute  $r$  band magnitude ( $M_r$ ) and is known to show a bimodal distribution (Bell et al. 2004). The  $(u - r)$  color represents the star formation rate (SFR) per unit stellar mass whereas  $M_r$  represents the stellar mass of a galaxy. The CMD is bimodal with the star forming galaxies lying in the bluer and hence lower part of the CMD whereas the redder galaxies with low SFRs are in the upper part of the CMD (Schawinski et al. 2014). These two regions are traditionally called the blue cloud and red sequence respectively, although other wavebands colors such as  $(NUV - r)$  have also been used (Salim et al. 2007).

Figure 6 shows the CMD of all the galaxies from the 681 galaxies, including galaxies in pairs of small groups. The total number is



**Figure 5.** Panel of a subset of 42 out of the 159 discovered Dual AGNs (with SDSS obj IDs listed)





**Figure 6.** The color magnitude diagram (CMD) of all 1393 galaxies in pairs of small groups (i.e. the total number of sources from the 681 galaxies in pairs and including their companions; a few are in groups of 3 or 4). A comparison sample of 743,379 SDSS galaxies (with clean photometric data available *i.e.*, having a value of 1 in the `clean` attribute of the galaxy’s corresponding entry in the `PhotoObjAll` table) at redshifts  $z < 0.5$  are plotted in grey scale. The integrated  $(u - r)$  colors corrected for extinction of the galaxies are plotted against their absolute magnitudes in the  $r$  band,  $M_r$ . Galaxies belonging to group having different number of companions are given different color (red for galaxies in group having 2 galaxies, blue for galaxies in group having 3 galaxies, yellow for galaxies in group having 4 galaxies) and are shown as individual colored points superimposed on a grey-scale contour map of the distribution of the comparison sample, where the darker shades represent the denser regions. The density contour levels are in units of the number of galaxies per grid unit of size 0.132 mag in  $M_r$  and 0.19 mag in  $(u - r)$ : 1500, 2250, 3000, 3500, 4200, 4800, 5400, 6000, 6600, 7000, 8000, 10000.

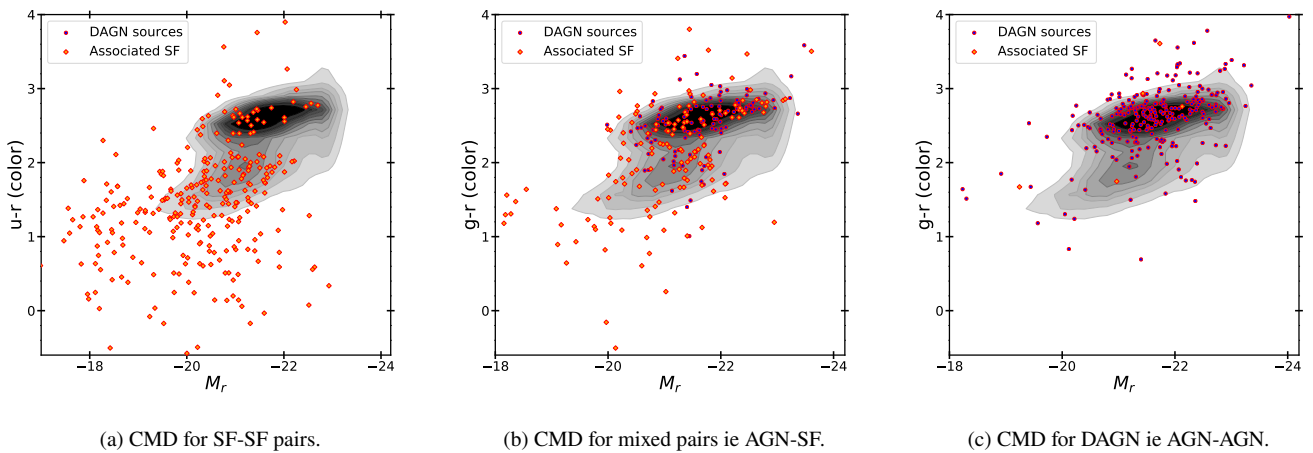


**Figure 7.** The 3 plots from left to right show respectively the relative positions of the star forming nuclei pairs (SF-SF), the mixed AGN-SF pairs and the DAGN on the CMD. The DAGN includes the two triple AGN.



1393. A comparison sample of 743379 SDSS galaxies with clean photometry flag at redshifts  $z < 0.499$  are plotted in grey scale. The integrated  $(u - r)$  colors of the galaxies are plotted against their absolute magnitudes in the  $r$  band  $M_r$ , after they were corrected for Galactic extinction. Galaxies belonging to group having different number of companions are given different color (red for galaxies in group having 2 galaxies, blue for galaxies in groups of 3 galaxies, black for groups of 4 galaxies) and are shown as individual colored points superimposed on a grey-scale contour map. It is interesting to see that a large fraction of the DNGs lie in the redder part of the CMD. This suggests that the star formation associated with the merging process is quenched as the nuclei come closer. The galaxies also have absolute magnitudes  $M_r < 18$  which suggests that the DNGs are associated with relatively more massive galaxies.

### 5.5 Estimating the fraction of DAGN in the 1 million sample

As shown in Section 5, applying GOTHIC to a sample of a million galaxies and the subsequent visual inspection results in a clean sample of 159 DAGN, all of which have spectroscopic confirmation. However, this is a lower limit and there are several ways in which “true” DAGN could have been missed in this process (e.g. spectroscopic data are not available, the components are closer than the minimum separation allowed by SDSS fibres, redshifts do not indicate pairs, noisy data). So it will be useful to have a ball park estimate of the number of DAGN expected in a sample of a million galaxies. This number will also tell us what is the number of DAGN we have missed in this study.

The number is difficult to estimate because many nuclei pairs can simply be due to the chance superposition of galaxies in the sky. But we can make a rough estimate of the upper limit to the expected number of DAGN based on the numbers we have obtained (see Figure 2).

(i) The total number of nuclei pairs that GOTHIC determines from the million galaxy sample is 95,159. The number with redshifts is 47,521 (*i.e.*, 49.93%), and from this sample 46,061 (96.92%) are close pairs within a fibre and 949 (*i.e.*, 1.99%) have separate redshifts. But the upper limit to the number of nuclei pairs that could be true close pairs is 95,159.

(ii) Since we need to estimate the number of expected DAGN we can use the fact that from the sample of 681 nuclei pairs we have detected 159 DAGN (as explained in Section 5). Hence the number of DAGN that could be expected from a one million sample =  $(159/681) \times 95,159 \approx 22,218$  DAGN (*i.e.*, 2.2%).

(iii) Since we have detected 159 DAGN from the sample, an upper limit to the fraction that we have missed is  $(22,218 - 159)/22,218 \approx 99.3\%$  approximately.

So DAGN are not only rare (2.2% predicted detection rate), but also difficult to detect. Mainly because many nuclei pairs could be due to superposition, large fraction of nuclei pairs lie within the SDSS fibre and a significant fraction of nuclei pairs do not have spectroscopic redshifts.

## 6 DISCUSSION

In this study we have discovered a new sample of dual/triple AGN, apart from mixed AGN-star forming nuclei pairs. We have used a novel algorithm named GOTHIC to automatically create a pool of DNGs and confirmed their nature using empirical relations such as those used in the BPT plot. Such algorithms are important for finding

SMBH pairs in large data sets (Mannucci et al. 2022). The final list of DAGN we obtained could be important inputs for models that predict the gravitation wave background from SMBH binaries (Casey-Clyde et al. 2022).

As discussed in the previous section, the number of DAGN that we expect (2.2%) in any galaxy population is much smaller than predicted in simulation studies (Volonteri et al. 2022; Bhowmick et al. 2020). Since the redshift distribution extends from  $z = 0$  to 0.7, this translates approximately to a typical projected separation of a few kpc at  $z = 0$  to a maximum of  $10''$  or 145kpc at  $z = 0.7$  (where  $H_0 = 70 \text{ km s}^{-1} \text{ Mpc}^{-1}$ ). The number of DAGN is 159, of which two are triple AGN. These numbers however, are lower limits, since we had to exclude nuclei pairs that lie within the SDSS fibre radius of  $1.5''$  as well as those that did not have good signal-to-noise ratio (S/N) spectroscopic data and so reliable emission line ratios could not be obtained. But overall these numbers suggest that dual/multiple AGN systems are not common (Table 2). The DAGN reported in the literature (Das et al. 2018) are often serendipitous in nature, and multi-wavelength surveys usually do not yield many DAGN (Rubinur et al. 2019). But AGN are known to produce winds/outflows that are important for building up the hot gas halos or CGM around galaxies and the presence of DAGN would increase this effect. Since the numbers of DAGN detected are relatively low, our results suggest that the starburst winds/outflows in galaxy mergers, and not just the DAGN, maybe be important for the growth of CGM around galaxies.

Another interesting implication of our study is that a large fraction of the DNGs and most of the DAGNs lie in the red cloud region of the galaxy color magnitude plot (Figure 6). To examine this in more detail we plotted the galaxy nuclei according to their type. Figure 7 shows the color magnitude diagram (CMD) for the different double nuclei pairs, star forming (SF-SF), mixed (AGN-SF) and DAGN. The SF-SF pairs lie over a wide range of colors ( $g - r$ ), with a significant fraction lying in the blue region of the CMD. Whereas the DAGN are mainly found in the red region of the CMD. So as one moves from SF-SF pairs to AGN-SF pairs and then finally to DAGN, the colors become redder with the DAGN nuclei lying in the reddest part of the CMD. This suggests that as the nuclei become redder during mergers (and perhaps come closer), star formation is quenched and AGN activity begins. Or perhaps AGN activity in DAGN quenches star formation. These effects have been observed in ultraluminous galaxies (ULIRGs) that are the result of gas rich major mergers and appear to be evolving into elliptical galaxies (Dasyra et al. 2006). In some cases their nuclei may give out radio jets and evolve into radio galaxies as well (Nandi et al. 2021).

The DAGN host galaxies are also more massive systems compared to the SF-SF and AGN-SF pair host galaxies. This indicates that the formation of the DAGN is the final stage in evolution of galaxy mergers and their nuclei. However, to understand this in more detail, the parameters of the nuclei, their separation and SMBH masses need to be determined. It will also be interesting to see how the DAGN evolve in cosmological simulations and if they show similar trends in the CMD. These questions will be followed up in our subsequent paper. Recall that 46,061 DNG detections were rejected in the third filtration process (Section 4.1), however, this rejected sample could also potentially contain DAGNs and could be studied further.

## 7 CONCLUSION

We present a novel detection algorithm called GOTHIC, that detects DNGs in given galaxy images from SDSS DR16. From this sample of DNGs, our goal was to find DAGN systems. The algorithm has been

tested on an existing catalog galaxy pairs that host double nuclei, and the results show a 100% detection rate. Subsequently, we applied GOTHIC on an *unknown* sample of one million galaxies that have spectroscopic data in SDSS DR16. From this sample, nearly 100,000 galaxies were reported to be DNG by GOTHIC. After careful filtration of the detected sample and removal of likely false detections, a small subset of 949 galaxies was studied visually to produce a confirmed sample of DAGN systems. We detected 681 nuclei pairs, and then used their emission line fluxes to determine their positions (AGN or star forming) on the BPT plot. The BPT showed that 159 are DAGN, of which 2 are triple AGN systems. The others are either star forming pairs (SF-SF) or AGN-star forming (AGN-SF) pairs. The color magnitude plot of the different nuclei pairs shows that the DAGN usually lie in galaxies that are redder and more massive compared to the SF-SF and AGN-SF pairs. Our results also suggest that DAGN may play a role in quenching star formation in galaxy mergers.

## ACKNOWLEDGEMENTS

The first author gratefully acknowledges the support received from the Indian Institute of Astrophysics, Bangalore, India during an internship. The second author also acknowledges the support of the Indian Institute of Astrophysics, Bangalore, India for a summer internship. M.Das acknowledges the support of the Science and Engineering Research Board (SERB) MATRICS grant MTR/2020/000266 for this research. S.Saha would like to thank the Science and Engineering research Board (SERB), Department of Science and Technology, Government of India, for supporting our research by providing us with resources to conduct our study. The project reference number is EMR/2016/005687.

Funding for the SDSS and SDSS-II has been provided by the Alfred P. Sloan Foundation, the Participating Institutions, the National Science Foundation, the U.S. Department of Energy, the National Aeronautics and Space Administration, the Japanese Monbukagakusho, the Max Planck Society, and the Higher Education Funding Council for England. The SDSS Web Site is <http://www.sdss.org/>. The SDSS is managed by the Astrophysical Research Consortium for the Participating Institutions. The Participating Institutions are the American Museum of Natural History, Astrophysical Institute Potsdam, University of Basel, University of Cambridge, Case Western Reserve University, University of Chicago, Drexel University, Fermilab, the Institute for Advanced Study, the Japan Participation Group, Johns Hopkins University, the Joint Institute for Nuclear Astrophysics, the Kavli Institute for Particle Astrophysics and Cosmology, the Korean Scientist Group, the Chinese Academy of Sciences (LAMOST), Los Alamos National Laboratory, the Max-Planck- Institute for Astronomy (MPIA), the Max-Planck-Institute for Astrophysics (MPA), New Mexico State University, Ohio State University, University of Pittsburgh, University of Portsmouth, Princeton University, the United States Naval Observatory, and the University of Washington.

## DATA AVAILABILITY

All the data upon which this work is based can be found at <https://github.com/anuwu/Blindtest-HQ>.

Nuclei ID	objID	Spectroscopic redshift (z)	u	r	Absolute r-band magnitude	class	subclass (SDSS)	subclass (BPT)
GTC_1_1	1237650762394959890	0.081	18.63	15.65	-22.31	GALAXY	BROADLINE	Seyfert
GTC_1_2	1237650762394959891	0.081	19.58	16.83	-21.12	GALAXY	...	Composite
GTC_2_1	1237651250964004981	0.102	20.31	17.51	-21.88	GALAXY	STARFORMING	Composite
GTC_2_2	1237651250964004982	0.102	19.82	17.48	-21.23	GALAXY	STARBURST	Composite
GTC_3_1	1237651252018151484	0.075	18.87	15.53	-22.44	GALAXY	...	Composite
GTC_3_2	1237651252018151487	0.075	19.52	16.17	-22.07	GALAXY	...	LINER
GTC_4_1	1237651252024377492	0.089	19.6	16.62	-21.59	GALAXY	...	LINER
GTC_4_2	1237651252024377493	0.089	19.8	16.8	-21.44	GALAXY	...	LINER
GTC_5_1	1237651273510289469	0.118	18.85	15.75	-22.95	GALAXY	...	LINER
GTC_5_2	1237651273510289470	0.119	20.64	17.93	-21.51	GALAXY	...	Composite
GTC_6_1	1237652600110383327	0.166	20.61	17.91	-20.81	GALAXY	STARFORMING	Composite
GTC_6_2	1237652600110383328	0.166	20.52	17.75	-20.90	GALAXY	...	Seyfert
GTC_7_1	1237652900234133595	0.200	21.76	17.74	-22.80	GALAXY	...	LINER
GTC_7_2	1237652900234133596	0.198	22.36	19.1	-20.18	GALAXY	STARFORMING	Composite
GTC_8_1	1237652946379604015	0.166	20.62	17.77	-22.05	GALAXY	...	Composite
GTC_8_2	1237652946379604014	0.164	20.74	16.83	-22.89	GALAXY	...	LINER
GTC_9_1	1237653441374453924	0.069	19.29	16.3	-21.34	GALAXY	STARFORMING	Composite
GTC_9_2	1237653441374453925	0.071	18.58	15.71	-21.56	GALAXY	...	Composite
GTC_10_1	1237654031400566817	0.040	18.01	15.05	-21.53	GALAXY	...	LINER
GTC_10_2	1237654031400566818	0.040	17.78	15.32	-22.48	GALAXY	STARFORMING	Composite
GTC_11_1	1237654382516240489	0.125	19.28	16.16	-23.25	GALAXY	...	LINER
GTC_11_2	1237654382516240490	0.123	20.23	16.98	-21.42	GALAXY	...	Seyfert
GTC_12_1	1237654880736968887	0.098	20.23	16.98	-21.01	GALAXY	...	Composite
GTC_12_2	1237654880736968888	0.098	19.29	17.33	-21.30	GALAXY	STARFORMING	Composite
GTC_13_1	1237655106765521018	0.114	19.39	16.26	-22.46	GALAXY	...	Composite
GTC_13_2	1237655106765521019	0.113	20.09	17.82	-21.33	GALAXY	...	Composite
GTC_14_1	1237655369279733929	0.073	19.67	16.98	-20.89	GALAXY	STARFORMING	Composite
GTC_14_2	1237655369279733928	0.074	18.5	16.07	-21.29	GALAXY	STARFORMING	Composite
GTC_15_1	1237655465384214778	0.074	18.04	15.07	-22.66	GALAXY	...	Composite
GTC_15_2	1237655465384214780	0.071	19.94	17.19	-21.68	GALAXY	...	Composite
GTC_16_1	1237655465920364786	0.098	20.15	17.06	-21.48	GALAXY	...	Seyfert
GTC_16_2	1237655465920364787	0.098	20.7	18.04	-20.67	GALAXY	...	Composite
GTC_17_1	1237655495979106559	0.091	20.11	17.34	-20.84	GALAXY	...	LINER
GTC_17_2	1237655495979106560	0.090	19.96	17.03	-20.96	GALAXY	STARFORMING	Composite
GTC_18_1	1237655692474515647	0.175	20.23	16.58	-23.35	GALAXY	...	LINER
GTC_18_2	1237655692474515648	0.174	20.56	17.86	-21.80	GALAXY	...	Composite
GTC_19_1	1237656239009104192	0.134	20.67	17.51	-21.83	GALAXY	...	LINER
GTC_19_2	1237656239009104193	0.133	20.99	17.29	-22.26	GALAXY	...	LINER
GTC_20_1	1237656567582294307	0.027	18.58	15.54	-21.74	GALAXY	...	Composite
GTC_20_2	1237656567582294308	0.026	18.77	16.24	-20.42	GALAXY	...	Composite
GTC_21_1	1237667253455356213	0.090	18.59	15.45	-22.32	GALAXY	...	Composite
GTC_21_2	<b>1237667253455356214</b>	0.091	22.51	19.36	...	GALAXY	...	LINER
GTC_22_1	1237656567585833094	0.057	17.99	14.97	-22.26	GALAXY	...	LINER
GTC_22_2	1237656567585833097	0.057	19.58	15.8	-21.95	GALAXY	...	Seyfert
GTC_23_1	1237656906354393114	0.023	16.66	14.01	-21.39	GALAXY	...	LINER
GTC_23_2	1237656906354393115	0.024	22.04	20.73	-19.56	GALAXY	STARFORMING	Composite
GTC_24_1	1237657189817516083	0.139	20.71	17.63	-22.55	GALAXY	...	LINER
GTC_24_2	1237657189817516085	0.138	22.1	18.3	-21.23	GALAXY	...	Composite
GTC_25_1	1237657221485625353	0.046	16.94	14.24	-21.66	GALAXY	BROADLINE	LINER
GTC_25_2	1237657221485559856	0.046	19.73	16.67	-21.01	GALAXY	...	LINER
GTC_26_1	1237657609104982532	0.153	20.17	17.06	-22.36	GALAXY	...	Seyfert
GTC_26_2	1237657609104982533	0.153	21.66	17.89	-21.68	GALAXY	...	LINER
GTC_27_1	1237657612874940605	0.070	19.36	16.32	-21.75	GALAXY	...	Composite
GTC_27_2	1237657612874940607	0.069	20.2	17.55	-20.80	GALAXY	...	Composite
GTC_28_1	1237657628432531602	0.078	18.91	15.74	-22.40	GALAXY	BROADLINE	LINER
GTC_28_2	1237657628432531603	0.078	20.36	17.13	-21.32	GALAXY	...	Composite

Nuclei ID	objID	Spectroscopic redshift (z)	u	r	Absolute r-band magnitude	class	subclass (SDSS)	subclass (BPT)
GTC_29_1	1237657857148911724	0.060	19.35	16.73	-20.17	GALAXY	...	LINER
GTC_29_2	1237657857148911725	0.060	18.6	16	-21.21	GALAXY	...	Composite
GTC_30_1	1237658300056338796	0.139	19.06	16.34	-21.83	GALAXY	STARFORMING	LINER
GTC_30_2	1237658300056338797	0.138	19.45	16.99	-22.02	GALAXY	...	Composite
GTC_31_1	1237658424090493080	0.072	19.34	16.62	-21.51	GALAXY	STARFORMING	Composite
GTC_31_2	1237658424090493081	0.071	19.15	16.23	-21.00	GALAXY	...	Composite
GTC_32_1	1237658611440222364	0.144	20.31	16.99	-22.66	GALAXY	...	LINER
GTC_32_2	1237658611440222365	0.145	20.84	17.62	-21.49	GALAXY	...	Composite
GTC_33_1	1237658918533005504	0.113	20.16	17.27	-21.40	GALAXY	...	Seyfert
GTC_33_2	1237658918533005505	0.113	20.56	17.87	-20.91	GALAXY	...	Composite
GTC_34_1	1237659119862939753	0.144	19.04	16.44	-21.67	GALAXY	STARFORMING	Composite
GTC_34_2	1237659119862939754	0.145	21.78	17.18	-22.39	GALAXY	...	Seyfert
GTC_35_1	1237659119864774675	0.099	19.37	15.84	-22.40	GALAXY	...	Composite
GTC_35_2	1237659119864774676	0.100	20.51	17.43	-21.18	GALAXY	...	Seyfert
GTC_36_1	1237659132206448648	0.110	21.07	17.87	-21.06	GALAXY	...	Seyfert
GTC_36_2	1237659132206448651	0.110	21.97	18.81	-20.22	GALAXY	...	Seyfert
GTC_37_1	1237660240313385134	0.142	21.95	18.23	-21.13	GALAXY	...	LINER
GTC_37_2	1237660240313385135	0.142	20.55	17.75	-20.68	GALAXY	STARFORMING	Composite
GTC_38_1	1237660240313712760	0.038	16.95	14.22	-21.57	GALAXY	STARFORMING	LINER
GTC_38_2	1237660240313712761	0.038	21.43	18.63	-19.41	GALAXY	...	Composite
GTC_39_1	1237660241385029806	0.074	19.27	16.32	-21.34	GALAXY	BROADLINE	LINER
GTC_39_2	1237660241385029810	0.073	20.12	17.54	-21.77	GALAXY	...	Composite
GTC_40_1	1237660669282812044	0.115	20.77	17.73	-21.19	GALAXY	...	LINER
GTC_40_2	1237660669282812045	0.116	20.93	17.85	-21.03	GALAXY	...	Seyfert
GTC_41_1	1237660963472932915	0.048	18.15	15.01	-22.37	GALAXY	...	LINER
GTC_41_2	1237660963472932916	0.048	18	15.57	-21.94	GALAXY	STARFORMING	Composite
GTC_42_1	1237661086415585604	0.047	15.96	13.14	-22.60	GALAXY	...	LINER
GTC_42_2	1237661086415585607	0.048	19.52	15.61	-22.33	GALAXY	...	Composite
GTC_43_1	1237661137963254106	0.129	19.75	16.6	-22.43	GALAXY	...	LINER
GTC_43_2	1237661137963254107	0.129	20.98	17.83	-21.78	GALAXY	...	LINER
GTC_44_1	1237661151377424586	0.104	20.6	16.58	-21.65	GALAXY	...	Composite
GTC_44_2	1237661151377424587	0.104	20.34	17.73	-20.64	GALAXY	...	Seyfert
GTC_45_1	1237661352706179107	0.082	18.21	15.82	-21.73	GALAXY	...	Composite
GTC_45_2	1237661352706179108	0.082	19.85	16.8	-21.47	GALAXY	...	Composite
GTC_46_1	1237661382778093715	0.069	18.16	15.3	-21.95	GALAXY	...	Composite
GTC_46_2	1237661382778093716	0.068	18.86	16.04	-21.48	GALAXY	BROADLINE	Composite
GTC_47_1	1237661418748444829	0.107	19.09	16.09	-22.00	GALAXY	...	LINER
GTC_47_2	1237661418748444830	0.107	19.94	16.95	-21.22	GALAXY	...	Seyfert
GTC_48_1	1237661812274233471	0.064	17.55	15.59	-22.10	GALAXY	STARBURST	Composite
GTC_48_2	1237661812274233472	0.064	19.4	16.41	-21.38	GALAXY	...	LINER
GTC_49_1	1237661813348106331	0.123	19.74	16.67	-22.04	GALAXY	...	Seyfert
GTC_49_2	1237661813348106332	0.124	20.7	17.74	-21.03	GALAXY	...	Composite
GTC_50_1	1237661850411204729	0.076	18.19	15.75	-21.96	GALAXY	STARFORMING	Composite
GTC_50_2	1237661850411204730	0.075	19.42	16.5	-21.49	GALAXY	...	Seyfert
GTC_51_1	1237661871330361452	0.112	19.47	16.36	-22.32	GALAXY	...	LINER
GTC_51_2	1237661871330361453	0.112	18.84	15.77	-22.72	GALAXY	...	Composite
GTC_52_1	1237661957762842806	0.133	20.94	17.21	-22.04	GALAXY	...	Composite
GTC_52_2	1237661957762842807	0.133	20.79	17.34	-21.58	GALAXY	...	Seyfert
GTC_53_1	1237661966886633584	0.131	20.61	17.27	-21.89	GALAXY	...	LINER
GTC_53_2	1237661966886633585	0.131	20.69	17.6	-21.82	GALAXY	...	LINER
GTC_54_1	1237661971721945220	0.073	19.22	16.23	-21.74	GALAXY	...	Seyfert
GTC_54_2	1237661971721945221	0.074	18.43	15.72	-21.23	GALAXY	...	LINER
GTC_55_1	1237662193453760669	0.171	20.6	17.6	-22.20	GALAXY	...	Composite
GTC_55_2	1237662193453760670	0.173	20.96	17.62	-22.01	GALAXY	...	Seyfert
GTC_56_1	1237662194541002843	0.073	18.36	15.47	-22.48	GALAXY	...	LINER
GTC_56_2	1237662194541002844	0.074	18.4	15.8	-21.54	GALAXY	...	Seyfert



Nuclei ID	objID	Spectroscopic redshift (z)	u	r	Absolute r-band magnitude	class	subclass (SDSS)	subclass (BPT)
GTC_57_1	1237662198280552769	0.172	21.03	17.62	-22.17	GALAXY	...	LINER
GTC_57_2	1237662198280552768	0.172	21.25	17.69	-22.25	GALAXY	...	LINER
GTC_58_1	1237662225666932750	0.099	20	16.83	-21.67	GALAXY	...	Composite
GTC_58_2	1237662225666932751	0.099	20.92	18.21	-20.28	GALAXY	...	Composite
GTC_59_1	1237662335178178801	0.065	18.45	15.57	-22.17	GALAXY	...	Seyfert
GTC_59_2	1237662335178178802	0.065	19.85	17.05	-20.85	GALAXY	...	Seyfert
GTC_60_1	1237662336792920258	0.069	18.99	16.25	-21.25	GALAXY	...	LINER
GTC_60_2	1237662336792920257	0.070	18.33	15.67	-21.27	GALAXY	STARFORMING	Composite
GTC_61_1	1237662474231021741	0.117	19.12	16.09	-22.85	GALAXY	...	LINER
GTC_61_2	1237662474231021742	0.117	20.26	17.23	-20.96	GALAXY	...	Composite
GTC_62_1	1237662498390737019	0.154	19.87	16.69	-22.60	GALAXY	...	LINER
GTC_62_2	1237662498390737020	0.153	20.01	16.95	-22.72	GALAXY	...	LINER
GTC_63_1	1237662200436752504	0.105	19.28	16.09	-22.49	GALAXY	...	LINER
GTC_63_2	1237662636375867758	0.105	19.86	16.8	-21.93	GALAXY	STARFORMING	Composite
GTC_64_1	1237662640123609565	0.059	18.42	15.48	-21.90	GALAXY	...	Composite
GTC_64_2	1237662640123609566	0.060	24.26	21.75	-20.71	GALAXY	...	Composite
GTC_65_1	1237663463145537628	0.084	17.15	13.92	-23.95	GALAXY	...	Seyfert
GTC_65_2	1237663463145537634	0.084	28.58	16.97	-24.36	GALAXY	...	LINER
GTC_66_1	1237663543683318057	0.084	19.87	17.1	-20.45	GALAXY	...	Composite
GTC_66_2	1237663543683318058	0.085	20.4	17.93	-20.57	GALAXY	STARFORMING	Composite
GTC_67_1	1237663782589432032	0.139	20.97	17.8	-21.66	GALAXY	...	Composite
GTC_67_2	1237663782589432033	0.139	20.78	17.8	-21.44	GALAXY	...	Composite
GTC_68_1	1237663783122370706	0.186	20.76	17.25	-22.73	GALAXY	...	LINER
GTC_68_2	1237663783122370707	0.183	22.18	18.77	-21.18	GALAXY	...	LINER
GTC_69_1	1237663783131283514	0.089	17.89	16.52	-20.21	GALAXY	STARBURST	Composite
GTC_69_2	1237663783131283515	0.089	19.53	16.59	-21.31	GALAXY	...	Composite
GTC_70_1	1237663783136985126	0.120	20.64	17.85	-20.38	GALAXY	...	Composite
GTC_70_2	1237663783136985125	0.121	20.12	17.05	-21.85	GALAXY	...	Seyfert
GTC_71_1	1237663783674183846	0.112	20.19	17.25	-21.09	GALAXY	STARFORMING	Composite
GTC_71_2	1237663783674183847	0.111	19.92	18.01	-20.16	GALAXY	STARFORMING	Composite
GTC_72_1	1237663784195653787	0.079	20.77	17.53	-21.71	GALAXY	...	LINER
GTC_72_2	1237663784195653788	0.079	19.68	17.67	-18.91	GALAXY	...	Composite
GTC_73_1	1237663784200831188	0.073	19.51	16.65	-21.10	GALAXY	...	LINER
GTC_73_2	1237663784200831189	0.074	19.8	17.48	-20.61	GALAXY	STARFORMING	Composite
GTC_74_1	1237663784739995886	0.115	19	16.79	-20.96	GALAXY	STARFORMING	Composite
GTC_74_2	1237663784739995887	0.116	20.39	17.38	-21.84	GALAXY	...	Composite
GTC_75_1	1237664291548823599	0.041	17.88	15.17	-21.74	GALAXY	BROADLINE	LINER
GTC_75_2	1237664291548823600	0.041	16.38	13.92	-21.74	GALAXY	...	LINER
GTC_76_1	1237664667352039631	0.084	20.13	17.08	-21.09	GALAXY	...	LINER
GTC_76_2	1237664667352039632	0.085	19.1	16.84	-21.23	GALAXY	STARFORMING	LINER
GTC_77_1	1237664817676484746	0.215	19.86	17.79	-22.19	GALAXY	STARFORMING	Composite
GTC_77_2	1237664817676484748	0.216	20.71	17.84	-21.76	GALAXY	STARFORMING	Composite
GTC_78_1	1237664871900577858	0.049	19.33	16.45	-21.01	GALAXY	...	LINER
GTC_78_2	1237664871900577859	0.051	19.73	17.07	-21.50	GALAXY	...	Seyfert
GTC_79_1	1237664877803077714	0.116	20.7	17.59	-21.25	GALAXY	...	LINER
GTC_79_2	1237664877803077715	0.118	20.59	17.43	-21.80	GALAXY	...	LINER
GTC_80_1	1237664877807927453	0.206	21.04	17.68	-22.63	GALAXY	...	Seyfert
GTC_80_2	1237664877807927454	0.207	22.19	17.62	-22.57	GALAXY	...	LINER
GTC_81_1	1237665103283814519	0.075	19.44	16.54	-21.57	GALAXY	...	LINER
GTC_81_2	1237665103283814520	0.075	18.36	15.57	-21.89	GALAXY	...	LINER
GTC_82_1	1237665129610936526	0.154	21.23	17.56	-21.86	GALAXY	...	LINER
GTC_82_2	1237665129610936527	0.153	21.66	17.89	-21.23	GALAXY	STARFORMING	Composite
GTC_83_1	1237665328779100316	0.154	21.21	17.63	-21.96	GALAXY	...	LINER
GTC_83_2	1237665328779100317	0.155	20.06	16.98	-22.56	GALAXY	...	Seyfert
GTC_84_1	1237665330927435873	0.088	19.2	16.48	-21.65	GALAXY	STARBURST	Composite
GTC_84_2	1237665330927435875	0.088	20.68	18.25	-19.99	GALAXY	...	Seyfert

Nuclei ID	objID	Spectroscopic redshift (z)	u	r	Absolute r-band magnitude	class	subclass (SDSS)	subclass (BPT)
GTC_85_1	1237665331455459378	0.072	18.09	15.84	-22.28	GALAXY	STARFORMING	Seyfert
GTC_85_2	1237665331455459379	0.073	18.13	17.16	-20.11	GALAXY	STARFORMING	Composite
GTC_86_1	1237665331457425465	0.128	19.99	16.62	-22.59	GALAXY	...	LINER
GTC_86_2	1237665331457425466	0.127	20.09	16.8	-22.65	GALAXY	...	LINER
GTC_87_1	1237665428091240506	0.140	18.97	16.27	-22.55	GALAXY	...	Seyfert
GTC_87_2	1237665428091240507	0.141	21.26	18.32	-20.88	GALAXY	...	Composite
GTC_88_1	1237665429713780966	0.088	20.43	17.5	-20.62	GALAXY	...	Composite
GTC_88_2	1237665429713846350	0.090	19.39	16.57	-21.76	GALAXY	...	LINER
GTC_89_1	1237665440439336990	0.065	17.45	14.57	-22.50	GALAXY	...	Composite
GTC_89_2	1237665440439336991	0.061	17.74	14.82	-22.30	GALAXY	...	LINER
GTC_90_1	1237665531723579489	0.132	19.47	16.37	-22.38	GALAXY	...	LINER
GTC_90_2	1237665531723579490	0.130	20.12	17.16	-21.66	GALAXY	...	LINER
GTC_91_1	1237665566082269200	0.094	18.86	15.76	-22.41	GALAXY	...	LINER
GTC_91_2	1237665566082269201	0.094	20.25	17.2	-21.29	GALAXY	...	Composite
GTC_92_1	1237666185634447638	0.121	21.03	17.64	-21.49	GALAXY	...	LINER
GTC_92_2	1237666185634447639	0.121	20.97	17.3	-22.01	GALAXY	...	LINER
GTC_93_1	1237666301627924604	0.156	23.1	19.58	-20.87	GALAXY	...	Composite
GTC_93_2	1237666301627924605	0.156	19.48	16.97	-21.76	GALAXY	STARFORMING	LINER
GTC_94_1	1237666407381598382	0.080	19.72	17.08	-21.20	GALAXY	STARFORMING	Composite
GTC_94_2	1237666407381598383	0.080	18.3	16.49	-19.44	GALAXY	...	Composite
GTC_95_1	1237667109574279383	0.201	21.18	17.51	-22.75	GALAXY	...	LINER
GTC_95_2	1237667109574279384	0.200	21.47	17.79	-22.40	GALAXY	...	Composite
GTC_96_1	1237667209974710300	0.078	19.19	17.4	-20.40	GALAXY	STARBURST	Composite
GTC_96_2	1237667209974710301	0.078	19.49	16.83	-21.00	GALAXY	STARFORMING	Composite
GTC_97_1	1237667212115050866	0.172	20.88	17.51	-22.48	GALAXY	...	LINER
GTC_97_2	1237667212115050867	0.173	21.84	18.38	-21.42	GALAXY	...	Composite
GTC_98_1	1237667212136284360	0.138	21.01	17.71	-21.44	GALAXY	...	LINER
GTC_98_2	1237667212136284359	0.130	19.49	17.03	-21.30	GALAXY	...	Seyfert
GTC_99_1	1237667253453324693	0.141	19.56	16.64	-21.99	GALAXY	...	LINER
GTC_99_2	1237667253453324694	0.141	21.16	17.11	-22.04	GALAXY	...	LINER
GTC_100_1	1237667254546006103	0.145	19.25	17.88	-20.04	GALAXY	STARFORMING	Composite
GTC_100_2	1237667254546006104	0.145	20.88	17.84	-20.48	GALAXY	...	LINER
GTC_101_1	1237667323250213040	0.038	17.99	15.28	-21.45	GALAXY	STARFORMING	Composite
GTC_101_2	1237667323250213041	0.038	19.77	18	-18.23	GALAXY	...	Composite
GTC_102_1	1237667323796127885	0.083	18.76	16.18	-21.58	GALAXY	...	LINER
GTC_102_2	1237667323796127886	0.083	20.04	17.47	-20.71	GALAXY	STARFORMING	Composite
GTC_103_1	1237667442437914759	0.079	19.57	16.64	-21.55	GALAXY	...	LINER
GTC_103_2	1237667442437914760	0.080	19.25	16.73	-21.25	GALAXY	STARFORMING	Composite
GTC_104_1	1237667549268148435	0.118	19.11	16.73	-21.37	GALAXY	STARFORMING	Composite
GTC_104_2	1237667549268213959	0.116	18.99	16.43	-21.31	GALAXY	STARFORMING	Composite
GTC_105_1	1237667733989949671	0.090	20.34	17.36	-21.04	GALAXY	...	Composite
GTC_105_2	1237667733989949676	0.089	20.39	17.31	-21.04	GALAXY	...	Seyfert
GTC_106_1	1237667734526886197	0.119	20.61	17.65	-21.30	GALAXY	...	Composite
GTC_106_2	1237667734526886198	0.118	20.44	17.08	-21.71	GALAXY	...	Seyfert
GTC_107_1	1237667736133828618	0.096	18.9	15.97	-22.06	GALAXY	...	Seyfert
GTC_107_2	1237667736133828619	0.097	18.99	16.07	-22.27	GALAXY	...	LINER
GTC_108_1	1237667781774934219	0.102	18.81	15.87	-21.80	GALAXY	...	Composite
GTC_108_2	1237667781774934220	0.103	20.42	17.3	-21.21	GALAXY	...	Seyfert
GTC_109_1	1237667783883817113	0.148	24.68	17.24	-22.41	GALAXY	...	LINER
GTC_109_2	1237667783883817114	0.149	20.12	17.55	-22.02	GALAXY	...	Seyfert
GTC_110_1	1237667783929299179	0.051	17.49	14.64	-22.07	GALAXY	BROADLINE	LINER
GTC_110_2	1237667783929299180	0.050	18.31	15.66	-21.49	GALAXY	BROADLINE	LINER
GTC_111_1	1237667910069190795	0.077	18.24	16.11	-21.18	GALAXY	STARFORMING	Composite
GTC_111_2	1237667910069190796	0.077	18.33	16.16	-22.39	GALAXY	STARFORMING	Composite
GTC_112_1	1237667916494012508	0.066	18.51	15.76	-21.44	GALAXY	...	Seyfert
GTC_112_2	1237667916494012509	0.065	18.69	15.76	-21.63	GALAXY	...	LINER

Nuclei ID	objID	Spectroscopic redshift (z)	u	r	Absolute r-band magnitude	class	subclass (SDSS)	subclass (BPT)
GTC_113_1	1237668271362211975	0.088	19.37	16.28	-22.22	GALAXY	...	LINER
GTC_113_2	1237668271362211976	0.089	19.78	17.1	-20.48	GALAXY	...	LINER
GTC_114_1	1237668298204446938	0.119	18.81	17.09	-21.83	GALAXY	STARBURST	Composite
GTC_114_2	1237668298204446939	0.119	20.7	16.93	-22.08	GALAXY	STARFORMING	Composite
GTC_115_1	1237668589722534078	0.153	20.55	17.59	-21.62	GALAXY	STARFORMING	Composite
GTC_115_2	1237668589722534074	0.152	21.45	17.98	-21.72	GALAXY	...	Composite
GTC_116_1	1237668623551103255	0.216	20.18	17.72	-22.03	GALAXY	...	Composite
GTC_116_2	1237668623551103256	0.216	23.16	18.94	-23.00	GALAXY	...	Composite
GTC_117_1	1237668672938115205	0.136	19.77	16.4	-22.48	GALAXY	...	LINER
GTC_117_2	1237668672938115206	0.135	21.01	17.89	-21.07	GALAXY	...	Composite
GTC_118_1	1237670964313456852	0.076	18.02	15.16	-22.48	GALAXY	...	LINER
GTC_118_2	1237670964313456853	0.078	18.52	15.61	-22.12	GALAXY	...	LINER
GTC_119_1	1237670965383266430	0.031	17.81	15.04	-21.53	GALAXY	...	LINER
GTC_119_2	1237670965383266433	0.030	18.18	15.57	-21.36	GALAXY	...	Composite
GTC_120_1	1237671931208925416	0.073	18.22	15.26	-22.37	GALAXY	...	LINER
GTC_120_2	1237671931208925417	0.073	19.75	16.78	-21.46	GALAXY	...	LINER
GTC_121_1	1237673807580693064	0.144	20.13	16.39	-22.88	GALAXY	...	LINER
GTC_121_2	1237673807580693069	0.140	20.46	17.37	-21.18	GALAXY	...	Composite
GTC_122_1	1237673808116122327	0.100	18.35	16.19	-21.85	GALAXY	STARFORMING	Composite
GTC_122_2	1237673808116122329	0.099	19.45	16.4	-21.40	GALAXY	...	LINER
GTC_123_1	1237674649921061067	0.096	19.22	16.11	-22.29	GALAXY	...	Composite
GTC_123_2	1237674649921061068	0.093	19.21	16.32	-21.94	GALAXY	...	Composite
GTC_124_1	1237657587096289353	0.025	16.62	13.89	-21.51	GALAXY	...	Seyfert
GTC_124_2	<b>1237657587096289354</b>	0.025	20.44	18.21	...	GALAXY	...	Seyfert
GTC_125_1	1237666210341978625	0.060	19.28	16.97	-20.89	GALAXY	STARFORMING	Composite
GTC_125_2	1237666210341978627	0.061	18.89	16.36	-21.33	GALAXY	STARFORMING	Composite
GTC_126_1	1237662335180341316	0.064	18.23	15.84	-21.52	GALAXY	STARFORMING	Composite
GTC_126_2	<b>1237662335180341327</b>	0.064	22.59	21.88	...	GALAXY	STARFORMING	Composite
GTC_127_1	1237659327092752463	0.149	18.81	17.52	-22.07	QSO	STARBURST	Seyfert
GTC_127_2	1237659327092752464	0.150	20.58	17.62	-21.56	GALAXY	STARFORMING	Composite
GTC_128_1	1237667915957665832	0.065	17.86	14.74	-22.90	GALAXY	...	Composite
GTC_128_2	1237667915957665835	0.065	18.1	15.24	-21.86	GALAXY	AGN	Composite
GTC_129_1	1237668588651282620	0.074	18.39	15.57	-21.94	GALAXY	...	LINER
GTC_129_2	1237668588651282621	0.074	18.24	15.76	-21.15	GALAXY	AGN	LINER
GTC_130_1	1237671262267506768	0.052	16.96	14.02	-22.83	GALAXY	AGN	LINER
GTC_130_2	1237671262267506767	0.053	19.53	16.73	-20.68	GALAXY	...	LINER
GTC_131_1	1237666227490586650	0.103	18.23	16.29	-22.30	GALAXY	STARBURST	Composite
GTC_131_2	1237666227490586649	0.104	20.69	17.95	-21.58	QSO	STARBURST	Composite
GTC_132_1	1237666228063371544	0.100	20.39	16.97	-21.91	GALAXY	AGN	Seyfert
GTC_132_2	1237666228063371545	0.099	18.16	16.08	-22.06	GALAXY	STARFORMING	Composite
GTC_133_1	1237667252917895553	0.153	20.31	16.48	-23.22	GALAXY	...	LINER
GTC_133_2	1237667252917895554	0.156	18.53	16.94	-22.36	QSO	STARBURST	Composite
GTC_134_1	1237664667360755820	0.152	19.89	18.03	-22.35	QSO	STARBURST	Composite
GTC_134_2	1237664667360755822	0.153	20.87	19.29	-18.30	GALAXY	AGN	Composite
GTC_135_1	1237660240314433647	0.156	20.74	17.5	-22.79	GALAXY	...	Seyfert
GTC_135_2	1237660240314433648	0.158	21.46	18.07	-21.43	GALAXY	AGN	Seyfert
GTC_136_1	1237655502962688659	0.030	17.75	15.16	-20.91	GALAXY	AGN	LINER
GTC_136_2	1237655502962688660	0.029	20.5	18.1	-22.72	GALAXY	STARFORMING	Composite
GTC_137_1	1237655465916104829	0.132	20.15	17.28	-21.32	GALAXY	AGN	LINER
GTC_137_2	1237655465916104830	0.132	21.25	17.5	-22.04	GALAXY	...	LINER
GTC_138_1	1237653616938516591	0.099	19.02	16.19	-21.58	GALAXY	AGN	LINER
GTC_138_2	1237653616938516592	0.099	19.86	16.84	-21.23	GALAXY	...	LINER
GTC_139_1	1237652600635851575	0.175	19.61	17.01	-22.90	GALAXY	AGN	LINER
GTC_139_2	1237652600635851576	0.178	20.45	17.13	-22.72	GALAXY	...	LINER
GTC_140_1	1237651250968461337	0.223	18.97	18.39	-21.39	QSO	STARBURST	Composite
GTC_140_2	1237651250968461338	0.223	24.15	20.53	-20.80	GALAXY	STARBURST	Composite

Nuclei ID	objID	Spectroscopic redshift (z)	u	r	Absolute r-band magnitude	class	subclass (SDSS)	subclass (BPT)
GTC_141_1	1237648721245503520	0.047	18.83	17.16	-21.21	GALAXY	STARBURST	Composite
GTC_141_2	1237648721245503521	0.048	17.92	15.52	-21.30	GALAXY	AGN	Seyfert
GTC_142_1	1237648722312888376	0.138	18.92	17.16	-21.79	GALAXY	STARBURST	Seyfert
GTC_142_2	1237648722312888377	0.138	19.79	17.08	-20.79	GALAXY	AGN	Seyfert
GTC_143_1	1237654382514471111	0.060	18.64	16.18	-20.81	GALAXY	AGN	Seyfert
GTC_143_2	1237654382514471112	0.060	19.48	17.05	-20.88	GALAXY	STARFORMING	Composite
GTC_144_1	1237657191979286606	0.087	19.23	16.06	-21.87	QSO	STARBURST	Seyfert
GTC_144_2	1237657191979286607	0.087	19.26	16.35	-21.78	GALAXY	...	LINER
GTC_145_1	1237659326018355482	0.105	19.69	16.7	-21.64	GALAXY	...	Seyfert
GTC_145_2	1237659326018355483	0.107	20.48	17.54	-21.64	GALAXY	AGN	Seyfert
GTC_146_1	1237661465992626516	0.063	19.53	16.54	-21.64	GALAXY	BROADLINE	LINER
GTC_146_2	1237661465992626517	0.065	19.36	16.22	-21.65	GALAXY	AGN	LINER
GTC_147_1	1237661812275347597	0.091	19.26	16.87	-21.56	GALAXY	AGN	Seyfert
GTC_147_2	1237661812275347598	0.092	20.65	17.72	-21.17	GALAXY	...	Composite
GTC_148_1	1237661813885436021	0.065	19.04	16.11	-21.43	GALAXY	...	LINER
GTC_148_2	1237661813885436022	0.065	19.33	16.79	-21.20	GALAXY	AGN	Seyfert
GTC_149_1	1237662224058089529	0.087	19.62	16.6	-21.79	GALAXY	...	Composite
GTC_149_2	1237662224058024149	0.088	19.78	16.77	-21.21	GALAXY	AGN	LINER
GTC_150_1	1237663542609117199	0.128	20.62	17.38	-22.12	QSO	STARBURST	Seyfert
GTC_150_2	1237663542609117200	0.128	20.71	17.11	-21.51	GALAXY	...	Composite
GTC_151_1	1237657192517926989	0.105	20.54	17.34	-21.28	GALAXY	...	LINER
GTC_151_2	1237657192517926990	0.106	22	18.94	-20.24	GALAXY	...	LINER
GTC_151_3	1237657192517926993	0.106	19.77	16.88	-21.83	GALAXY	...	Seyfert
GTC_152_1	1237661064950710579	0.126	19.37	16.03	-22.85	GALAXY	...	Composite
GTC_152_2	1237661064950710580	0.125	19.63	16.71	-22.17	GALAXY	...	LINER
GTC_152_3	<b>1237661064950710581</b>	0.127	21.28	18.91	...	GALAXY	...	...
GTC_153_1	1237663275777392799	0.094	21.26	18.1	-20.84	GALAXY	...	Composite
GTC_153_2	1237663275777392800	0.095	19.29	16.13	-22.01	GALAXY	...	Seyfert
GTC_153_3	1237663275777392798	0.091	20.77	17.53	-21.43	GALAXY	...	SF
GTC_154_1	1237663542608920721	0.144	21.47	17.59	-22.03	GALAXY	...	LINER
GTC_154_2	1237663542608920724	0.144	24.33	20.2	-21.12	GALAXY	...	Seyfert
GTC_154_3	1237663542608920720	0.144	22.06	17.82	-21.73	GALAXY	...	SF
GTC_155_1	1237663783126237343	0.063	19.48	16.54	-21.29	GALAXY	...	Composite
GTC_155_2	1237663783126237344	0.064	19.51	16.44	-21.49	GALAXY	...	LINER
GTC_155_3	1237663783126237342	0.064	18.34	15.34	-22.12	GALAXY	...	SF
GTC_156_1	1237665564997714246	0.260	21.57	18.18	-22.63	GALAXY	...	LINER
GTC_156_2	1237665564997779740	0.254	21.74	16.69	-24.02	GALAXY	...	Composite
GTC_156_3	1237665564997714249	0.254	24.19	18.2	-22.67	GALAXY	...	...
GTC_157_1	1237668299280089194	0.063	18.38	15.41	-22.07	GALAXY	...	LINER
GTC_157_2	1237668299280089196	0.063	19.45	16.93	-21.01	GALAXY	STARFORMING	Composite
GTC_157_3	1237668299280089195	0.062	18.57	15.73	-21.64	GALAXY	...	...
GTC_158_1	1237667736133107729	0.102	19.05	16.05	-22.55	GALAXY	...	Seyfert
GTC_158_2	1237667736133107730	0.103	18.99	15.96	-22.82	GALAXY	...	LINER
GTC_158_3	1237667736133107731	0.103	19.98	16.84	-21.44	GALAXY	BROADLINE	...
GTC_159_1	1237666301093675376	0.086	19.37	16.76	-21.31	QSO	BROADLINE	LINER
GTC_159_2	1237666301093675377	0.087	20.96	18.27	-19.72	GALAXY	...	LINER
GTC_159_3	1237666301093675378	0.088	19.88	17.87	-20.96	GALAXY	STARBURST	SF
GTC_159_4	1237666301093675379	0.086	20.92	18.99	-19.24	GALAXY	STARFORMING	SF

Table 3: Data from SDSS DR16 for all the DAGN objects identified by GOTHIC. There are 4 objects (marked in bold) whose absolute r-band magnitude values are missing. In SDSS object explorer, one of them is flagged to have unreliable photometric data and the others have related photometric flags which could explain their missing data.



## REFERENCES

- Aggarwal K., et al., 2019, *ApJ*, **880**, 116
- Baldwin J. A., Phillips M. M., Terlevich R., 1981, *PASP*, **93**, 5
- Barton E. J., Geller M. J., Kenyon S. J., 2000, *ApJ*, **530**, 660
- Bell E. F., et al., 2004, *ApJ*, **608**, 752
- Bellovary J. M., Governato F., Quinn T. R., Wadsley J., Shen S., Volonteri M., 2010, *ApJ*, **721**, L148
- Bhowmick A. K., Di Matteo T., Myers A. D., 2020, *MNRAS*, **492**, 5620
- Bickley R. W., et al., 2021, *MNRAS*, **504**, 372–392
- Blumenthal K. A., et al., 2019, *MNRAS*, **492**, 2075
- Bottrell C., et al., 2019, *MNRAS*, **490**, 5390
- Bottrell C., Hani M. H., Teimoorinia H., Patton D. R., Ellison S. L., 2021, *MNRAS*,
- Bustamante S., Ellison S. L., Patton D. R., Sparre M., 2020, *MNRAS*, **494**, 3469
- Canny J., 1986, *IEEE Transactions on Pattern Analysis and Machine Intelligence*, PAMI-8, 679
- Capelo P. R., Dotti M., Volonteri M., Mayer L., Bellovary J. M., Shen S., 2017, *MNRAS*, **469**, 4437
- Casey-Clyde J. A., Mingarelli C. M. F., Greene J. E., Pardo K., Nañez M., Goulding A. D., 2022, *ApJ*, **924**, 93
- Ciurlo A., et al., 2023, *A&A*, **671**, L4
- Das M., Rubinur K., Kharb P., Varghese A., Novakkuni N., James A., 2018, *Bulletin de la Societe Royale des Sciences de Liege*, **87**, 299
- Dasyra K. M., et al., 2006, *ApJ*, **651**, 835
- Davies J. J., Crain R. A., Oppenheimer B. D., Schaye J., 2020, *MNRAS*, **491**, 4462
- De Rosa A., et al., 2019, *New Astron. Rev.*, **86**, 101525
- Dressler A., 1984, *ARA&A*, **22**, 185
- Ellison S. L., Patton D. R., Simard L., McConnachie A. W., Baldry I. K., Mendel J. T., 2010, *MNRAS*, **407**, 1514
- Fernandes R. C., Stasińska G., Schlickmann M. S., Mateus A., Asari N. V., Schoenell W., Sodr e L. J., (the SEAGal collaboration) 2010, *MNRAS*, **403**, 1036
- Fielding D. B., et al., 2020, *ApJ*, **903**, 32
- Gimeno G. N., D az R. J., Carranza G. J., 2004, *The Astronomical Journal*, **128**, 62
- Goulding A. D., Pardo K., Greene J. E., Mingarelli C. M. F., Nyland K., Strauss M. A., 2019, *ApJ*, **879**, L21
- Greene J. E., et al., 2021, *ApJ*, **917**, 17
- Hopkins P. F., Kocevski D. D., Bundy K., 2014, *MNRAS*, **445**, 823
- J nsson H., et al., 2020, *AJ*, **160**, 120
- Juneau S., et al., 2014, *ApJ*, **788**, 88
- Kauffmann G., et al., 2003, *MNRAS*, **346**, 1055
- Kewley L. J., Groves B., Kauffmann G., Heckman T., 2006, *MNRAS*, **372**, 961
- Kharb P., Lal D. V., Merritt D., 2017a, *Nature Astronomy*, **1**, 727
- Kharb P., Subramanian S., Vaddi S., Das M., Paragi Z., 2017b, *ApJ*, **846**, 12
- Kim E., et al., 2021, *MNRAS*, **507**, 3113
- Komossa S., Burwitz V., Hasinger G., Predehl P., Kaastra J. S., Ikebe Y., 2003, *ApJ*, **582**, L15
- Koss M., Mushotzky R., Veilleux S., Vasudevan R., Miller N., Sanders D. B., Schawinski K., Trippel M., 2011, *ApJ*, **735**, L42
- Koss M., Mushotzky R., Treister E., Veilleux S., Vasudevan R., Trippel M., 2012, *ApJ*, **746**, L22
- Koss M. J., et al., 2023a, *ApJ*, **942**, L24
- Koss M. J., et al., 2023b, *The Astrophysical Journal Letters*, **942**, L24
- Makhija S., Saha S., Basak S., Das M., 2019, *Astronomy and Computing*, **29**, 100313
- Mannucci F., et al., 2022, *Nature Astronomy*, **6**, 1185
- Maschmann D., Melchior A.-L., Mamon G. A., Chilingarian I. V., Katkov I. Y., 2020, *A&A*, **641**, A171
- Mazzarella J. M., et al., 2012, *AJ*, **144**, 125
- Mezcua M., Lobanov A. P., Mediavilla E., Karouzos M., 2014, *ApJ*, **784**, 16
- Nandi S., Das M., Dwarakanath K. S., 2021, *MNRAS*, **503**, 5746
- Nelson D., et al., 2019, *Computational Astrophysics and Cosmology*, **6**, 2
- Nevin R., Blecha L., Comerford J., Greene J., 2019, *ApJ*, **872**, 76
- Patton D. R., Atfield J. E., 2008, *ApJ*, **685**, 235
- Patton D. R., Qamar F. D., Ellison S. L., Bluck A. F. L., Simard L., Mendel J. T., Moreno J., Torrey P., 2016, *MNRAS*, **461**, 2589
- Patton D. R., et al., 2020, *MNRAS*, **494**, 4969
- Peterson B. M., 1997, *An Introduction to Active Galactic Nuclei*. Cambridge University Press
- Reines A. E., Condon J. J., Darling J., Greene J. E., 2020, *ApJ*, **888**, 36
- Ricarte A., Tremmel M., Natarajan P., Zimmer C., Quinn T., 2021, *MNRAS*, **503**, 6098
- Rubinur K., Das M., Kharb P., 2018, *Journal of Astrophysics and Astronomy*, **39**, 8
- Rubinur K., Das M., Kharb P., 2019, *MNRAS*, **484**, 4933
- Rubinur K., Kharb P., Das M., Rahna P. T., Honey M., Paswan A., Vaddi S., Murthy J., 2020, *MNRAS*,
- Salim S., et al., 2007, *ApJS*, **173**, 267
- Sanders D. B., Mirabel I. F., 1996, *ARA&A*, **34**, 749
- Schawinski K., et al., 2014, *MNRAS*, **440**, 889
- Scialpi M., et al., 2023, *arXiv e-prints*, p. arXiv:2305.11850
- S rsic J. L., 1963, *Bulletin of the Argentine Association of Astronomy*, **6**, 41
- Shannon R. M., et al., 2015, *Science*, **349**, 1522
- Shlosman I., Begelman M. C., Frank J., 1990, *Nature*, **345**, 679
- Stemo A., Comerford J. M., Barrows R. S., Stern D., Assef R. J., Griffith R. L., Schechter A., 2021, *ApJ*, **923**, 36
- Thomas D., Maraston C., Bender R., Mendes de Oliveira C., 2005, *ApJ*, **621**, 673
- Tub n D., et al., 2021, *ApJ*, **911**, 100
- Volonteri M., Pfister H., Beckmann R., Dotti M., Dubois Y., Massonneau W., Musoke G., Tremmel M., 2022, *MNRAS*, **514**, 640
- White S. D. M., Rees M. J., 1978, *MNRAS*, **183**, 341
- Williams J., Koss M., Mushotzky R., Stern D., Treister E., Harrison F., Blecha L., 2021, in *American Astronomical Society Meeting Abstracts*. p. 209.08
- Yadav J., Das M., Barway S., Combes F., 2021, *A&A*, **651**, L9
- Yuan T. T., Kewley L. J., Sanders D. B., 2010, *ApJ*, **709**, 884
- Zhou H., Wang T., Zhang X., Dong X., Li C., 2004, *ApJ*, **604**, L33

# Supplementary Material to “Automated Detection of Double Nuclei Galaxies in SDSS using GOTHIC and Discovery of a Large Sample of Dual AGN”

arXiv:2011.12177v4 [astro-ph.GA] 11 Jul 2023

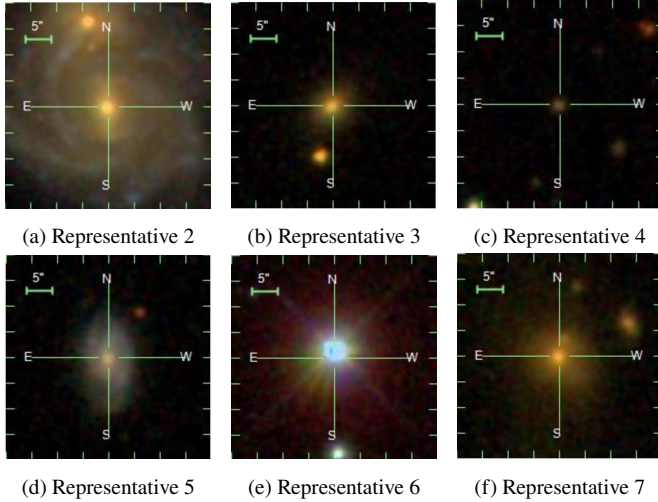


**Figure 1.** Representative sample of SDSS images seen in a blind search

## 1 DESCRIPTION OF THE PROCEDURE

We primarily describe the GOTHIC algorithm by means of example. In Table 1, we present a list of objIDs from SDSS that are representative of the images of galaxies seen in practice. In the remainder of this document, we refer to the  $n^{\text{th}}$  representative galaxy as “Rep  $n$ ”. The cutouts of each of these representatives are in Figure 1 which displays Rep 2 through 7. Rep 1 is the archetypal double nuclei Galaxy MRK 739 which is shown in Main Figure 1. <sup>1</sup>

We also provide algorithmic details of the sub-components of GOTHIC. For each sub-procedure below, we categorically state the representatives chosen for its demonstration along with grayscale images demonstrating the functionality of the sub-procedure. The coordinate axes of all grayscale images are scaled in pixels. Although we are interested in detecting galaxies only, we refer to the astronomical entity pointed to by an objID as an “object” for ease of describing the GOTHIC algorithm.

### 1.1 Image Normalization and Smoothing

#### Representative Chosen - 1

Every object must be appropriately treated so that it is amenable for classification. Using `astropy` (Price-Whelan et al. 2018), a 40''

<sup>1</sup> The hyperlink to the image of Rep1 is unavailable in the table. Please refer to the main text

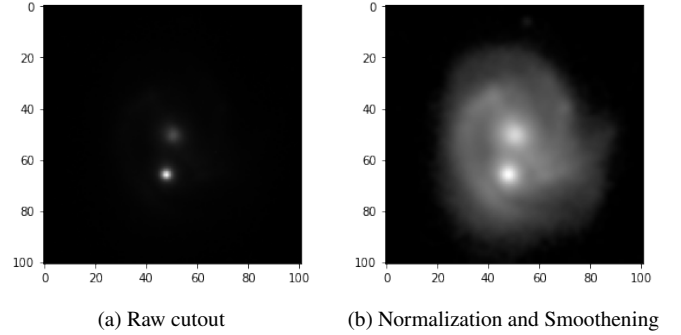


**Figure 2.** The raw and normalized SDSS cutouts for Rep 1

cutout centred on an object’s coordinates is performed. Note that the angular size of 40'' typically corresponds to 100 pixels. Thus the cutout images are of size 100 × 100 in terms of pixels. The raw cutout of Rep 1 is shown in Figure 2a. However, the light envelope of the galaxy and the dark background are not amenable for further analysis. The nuclei at the centre of the galaxy are faint and the body of the galaxy is not visible.

To resolve this issue, we perform a log normalization of all pixel values in the cutout followed by appropriate scaling of the image within the range of [0, 255]. Subsequently, we perform Gaussian smoothing using a kernel with standard deviations of  $(\sigma_x, \sigma_y) = (5, 5)$ . The resulting image is shown in Figure 2b.

### 1.2 Bounding the Galaxy via Edge Detection and Convex Hull

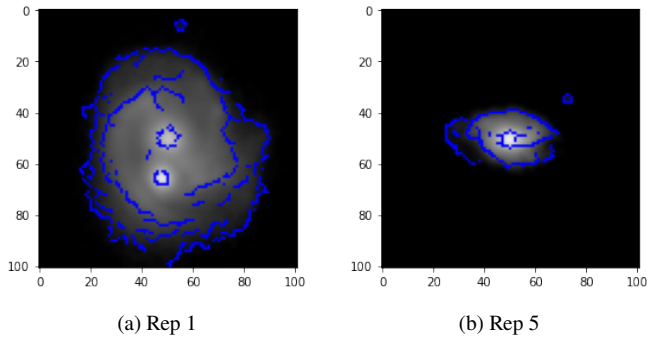
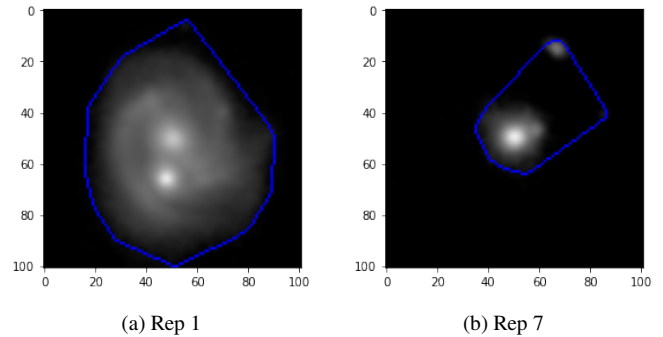
#### Representatives chosen - 1, 5, 7

Determining whether a galaxy is a DNG requires a reliable detection of two individual bright bulges within a galaxy envelope. Hence, it is important to determine the light envelope of the galaxy within which the search for dual peaks will take place. We use the Canny (Canny 1986) edge detection technique, which utilizes the Sobel (Vincent & Folorunso 2009) operator to create a discrete approximation of  $\frac{\partial}{\partial x}$  and  $\frac{\partial}{\partial y}$  at each pixel in the image, denoted by  $\Delta p_x, \Delta p_y$  respectively. Subsequently, the magnitude  $\sqrt{\Delta p_x^2 + \Delta p_y^2}$  is computed which represents how strongly a particular pixel is an edge.

For example, Figure 3a and Figure 3b show the edges detected by Canny (in blue) for Reps 1, 5 respectively. It is to be noted that Canny detects edges within the light envelope of the galaxy. This is expected since the Sobel operator measures the difference between neighboring pixel values at a given pixel coordinate. Generally, light

**Table 1.** List of representative objIDs

No.	objID	Common Name	Description	Figure
1	<a href="#">1237667734504407133</a>	MRK 739	Standard example of DNG	Main Figure 1
2	<a href="#">1237666301638279613</a>	UGC 3141	DNG with nuclei far apart. This example has been chosen to demonstrate the limits of <i>GOTHIC</i> .	1a
3	<a href="#">1237651752385708153</a>	2MASX J09520344+0052159	Single nucleus galaxy with a star in the foreground. Such samples are potential false positives.	1b
4	<a href="#">1237648720143647179</a>	SDSS J095203.44+005216.3	The frame does not contain sufficiently bright objects which can be detected by <i>GOTHIC</i> . Many objIDs in the blind search corresponding to such frames.	1c
5	<a href="#">1237650794609246465</a>	SDSS J094333.74-010551.3	Single nucleus galaxy. These are the most commonly encountered objects in a blind search. Hence it's important to verify that they are reliably identified.	1d
6	<a href="#">1237648720688971816</a>	SDSS J111508.35-003125.0	Star mislabelled as a galaxy in SDSS which we frequently encountered in the blind search. Hence it is a clear representative.	1e
7	<a href="#">1237650796756926591</a>	2MASS J09450600+0034516	Two galaxies in the same line of sight. Similar to representative 3, this is a potential source of false-positives.	1f

**Figure 3.** Edges detected by Canny**Figure 4.** Convex Hull of the Edges

profiles of galaxies in SDSS are not smooth and this causes sizeable differences between pixel values even within the light envelope which are mistakenly detected as edges.

We reiterate that the Gaussian Smoothing step in Section 1.1 is necessary as it reduces the detection of false edges within the light envelope. If the smoothing step were skipped, the Canny algorithm would detect far more edges than necessary. On the other hand, excessive smoothing using higher values of  $(\sigma_x, \sigma_y)$  would lead to no edges being detected. To resolve this issue, we find the convex hull of the pixel coordinates that have been detected as edges. The hulls for Reps 1 and 7 are shown in Figure 4a and Figure 4b respectively. Formally, the convex hull of a set of points  $\mathcal{S} = \{(x, y)\}$  in 2-D is the smallest convex polygon that contains in its interior all points in  $\mathcal{S}$ . Sklansky (1982) and Cormen et al. (2009) present an overview of the Convex Hull problem and efficient algorithms for computing it.

Note that the hull in Figure 4b encloses a neighboring object. However, it is clear that this object is not of interest to us. In other words, we assume that the enclosed hull contains more objects that are of interest to us merely due to them being in the line of sight. Since our cutout size is  $40''$ , it is reasonable to expect the actual object referenced by the objID would have many other objects in their line of sight and they need to be appropriately differentiated. Otherwise it can lead to unnecessarily high false-positive detections since two distinct objects that happen to be close together can be easily mistaken for a DNG. The sub-procedures in Section 1.3, Section 1.4 and part of Section 1.6 are dedicated to deal with such ‘‘line of sight’’ scenarios.

### 1.3 Numerical Fitting of the Galaxy Light Profile

#### Representatives Chosen - 1

Since the convex hull might enclose a larger area than the object of interest, it needs to be ascertained what portion of the image within the hull resembles a galaxy envelope. In Figure 4b, approximately one half of the hull (at the centre of the square image) contains the galaxy. This patch of light needs to be identified from the remainder of the hull. Next, we require a formal procedure for identifying the object of interest from the interior of the hull.

We make the assumption that the enclosed hull would always contain our galaxy of interest as well as other objects within the line of sight. The light profile of galaxies typically follow a distribution given by Sérsic (1963). This fact can be exploited to develop a procedure that separates a galaxy from the rest of the hull. Hence, we hypothesize that the pixel values in the hull will follow the Sérsic distribution. The expression for the Sérsic profile is as follows

$$\log I(R) = \log I_0 - kR^{\frac{1}{n}} \quad (1)$$

where  $I(R)$  is the light intensity of a galaxy as a function of the radial distance  $R$  from the galactic centre. The parameter  $n$  is known as the Sérsic index and it characterizes the overall shape of the light distribution. Caon et al. (1993) states that  $1 \leq n \leq 15$  fits the light profile of most galaxies. However, we have found that setting  $0.25 \leq n \leq 15$  works better in practice.

#### 1.3.1 Radius to Frequency Relation

The Sérsic profile is traditionally stated in terms of the radius from the galactic centre (Equation 1). However, this information is not

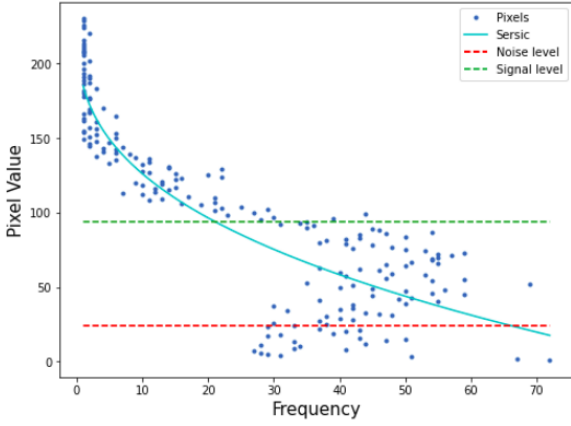


Figure 5. Rep 1 Sérsic Fit

readily calculable and moreover, it is unsuitable for fitting to the data available at hand *i.e.*, the image histogram. As a simple heuristic, we use the taxicab norm of the pixel coordinates to represent the radial distance from the galactic centre. The taxicab norm  $R$  of the point  $(x, y)$  is  $R = |x| + |y|$ .

In order to translate the taxicab radius  $R$  (which appears as the independent variable in the Sérsic equation) into frequency  $f$  (which is the data available to us). To find the relation from  $R \rightarrow f$ , we need to find the number of distinct points  $(x, y)$  that satisfy  $|x| + |y| = R$  for a given  $R$ . It can be shown that the relation is  $f = 4R$ .

### 1.3.2 Fitting the Image Histogram

We denote the histogram function of the smoothed image as  $F \equiv F(p)$  which translates pixel values to their corresponding frequency values. Let the inverse histogram be  $P \equiv P(f)$  that translates frequency numbers to pixel values of the smoothed image. The FITS files in SDSS report pixel values in a unit of flux called nanomaggies. It is these raw pixel values that are log-normalized and hence  $P(f)$  would be in the form of (Equation 1) apart from a constant additive factor. Hence, the  $P(f)$  would have the form

$$P(f; k, n) = P_{max} - k \left( \frac{f}{4} \right)^{\frac{1}{n}} \quad (2)$$

The term  $P_{max}$  is the largest pixel value within the hull. The form of (Equation 2) implicitly assumes that the pixel with the maximum value belongs to our object of interest and not a neighboring object. However, in practice if this assumption were not true, it would not affect the result significantly. This is because (Equation 2) is numerically fit to the histogram data from the hull and the process of numerical fitting averages over the statistical noise in the data. Such errors would be present even if our assumption of the maximum pixel value belonging to our object of interest were not true. In other words, from the point of view of numerical fitting, the fact that the assumption is false can simply be interpreted as a form of statistical noise; hence it does not affect the final outcome.

$P(f)$  is numerically fitted to the observed histogram to obtain the best-fit values for its parameters  $k, n$ . We use the `optimize.curve_fit` function from `scipy` (Virtanen et al. 2020) to perform the numerical fitting. We show the fitted curve to the observed histogram of Rep 1 in Figure 5. The blue dots are the observed pixel values from the smoothed image and the teal line is the numerically fitted curve  $P(f)$ .

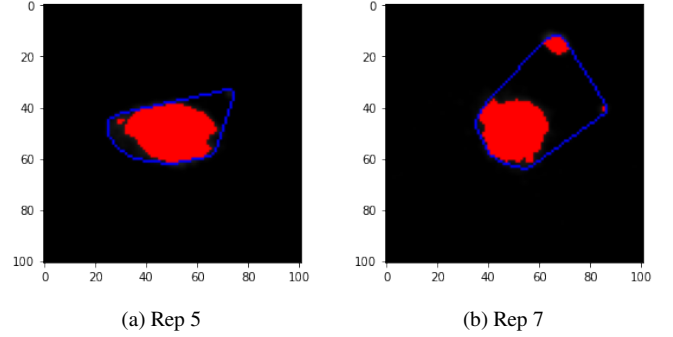


Figure 6. Search Region

## 1.4 Determination of the Search Region

### Representatives Chosen - 1, 5, 7

After the curve  $P(f)$  has been fitted to the histogram, it remains to be determined what pixel value separates the galaxy envelope from the background. This pixel value is known as the *cutoff level*. It is also required in the ambient noise calculation (Section 1.5). With respect to the function  $P(f)$ , the pixel value whose corresponding frequency value captures 95% of the total integrated light is chosen as the cutoff level.

Mathematically, a typical  $P(f)$  curve is a function of  $f$  from 0 to some maximum frequency value  $f_{max}$ . Thus, we define the following function

$$I_{integrated}(f) = \int_0^f P(f') df' \quad (3)$$

The total integrated light would be

$$I_{total} = I_{integrated}(f_{max}) \quad (4)$$

As per our definition, The cutoff level would then be  $P(f_{95})$  where  $f_{95}$  satisfies

$$I_{integrated}(f_{95}) = 0.95 \times I_{total} \quad (5)$$

We also define a *signal level* as  $P(f_{50})$ . The definition of  $f_{50}$  is analogous to that of  $f_{95}$  above. The signal level is not used in determining the search region, but is crucial in the final classification phase (Section 1.6)

With reference to Figure 5, the red line corresponds to the cutoff level and the green line is the signal level. All integral values mentioned are computed by numerically integrating the fit histogram  $P(f)$  using the composite trapezoidal rule (Talvila & Wiersma 2012) whilst dividing the range of  $[0, f_{max}]$  into 10,000 steps.

Figure 6a and Figure 6b show in red the region above the cutoff level. This is the *search region* where we look for dual peaks of light that characterizes DNGs. Note that the search region is included within the hull, and it perfectly masks the galaxy envelope (compare with Figure 1d and Figure 1f for reference). However, neighboring objects are mistakenly included at times within the envelope since their pixel values are above the cutoff (Figure 6b). The techniques in Section 1.6 handle such scenarios.

## 1.5 Iterated Hill Climbing

### Representatives chosen - 1, 2, 3



HILL-CLIMB( $pt, reg, img$ )

```

1   $newpt \leftarrow \text{NULL}$ 
2  while  $pt \neq newpt$ 
3      do  $neighs \leftarrow \text{GET-NEIGHBORS}(pt, 3, reg)$ 
4           $newpt \leftarrow pt$ 
5          for  $n$  in  $neighs$ 
6              do if  $img[n.x, n.y] > img[newpt.x, newpt.y]$ 
7   $pt \leftarrow newpt$ 
8  return  $newpt$ 

```

ITERATED-HILL-CLIMB( $reg, img$ )

```

1   $peak\_list \leftarrow \Phi$ 
2   $i \leftarrow 0$ 
3  repeat  $pt \leftarrow \text{CHOOSE-RANDOM}(reg)$ 
4       $peak \leftarrow \text{HILL-CLIMB}(pt, reg, img)$ 
5       $c_1 \leftarrow peak$  not in  $peak\_list$ 
6       $c_2 \leftarrow \text{SNR}(peak) \geq 3$ 
7       $neighs \leftarrow \text{GET-NEIGHBORS}(pt, 3, reg)$ 
8       $c_3 \leftarrow \text{INTERSECTION}(neighs, peak\_list) \text{ is } \Phi$ 
9      if  $c_1$  and  $c_2$  and  $c_3$ 
10         then  $\text{APPEND}(peak, peak\_list)$ 
11          $i \leftarrow i + 1$ 
12 until  $i = 1,000$ 
13 return  $peak\_list$ 

```

Having identified the galaxy envelope, we need to test for the presence of dual peaks of light which is characteristic of a DNG. However, a robust peak finding algorithm is first essential. We used a variant of the traditional hill-climbing algorithm to find the peaks. The idea is to start at a random pixel in the search region and then find the neighboring pixel which has the greatest pixel value. This process is repeated until no neighbor with a higher pixel value can be found. The final pixel at the end of this iterative process is reported to be the peak, provided the pixel value of the peak is greater than the *signal* level (Section 1.4) and the SNR ratio at the peak is  $> 3$ .

### 1.5.1 Noise Level Inference for SNR Calculation

To determine the noise level in the SNR calculation, we averaged over a randomly chosen  $3 \times 3$  grid of pixel values outside the convex hull. It needs to be ensured however that all constituent pixels of this chosen grid has pixel values below the cutoff level. This is done so that unrelated emissions that fall within the cutout do not erroneously influence the noise level inference.

In Main Section 4.2, we have provided justifications for using a spectroscopic sample. Many objects in SDSS that are classified as a ‘‘GALAXY’’ are actually foreground stars. These objects contaminate our initial blind sample, and thus to avoid them, we have chosen a spectroscopic sample. It is worthwhile to note how the noise inference would take place for such *contaminant* objects. They tend to have large diffraction spikes that permeates the entire region of the cutout. Hence, there may not be any  $3 \times 3$  grid in the image that is below the noise level. Moreover, performing fitting a Sérsic profile (Section 1.4) to a star is not scientifically sound (Sérsic light profiles are meant to fit to spiral/elliptical galaxies). In other words, contaminant foreground stars typically have cutout images whose features are not amenable to numerical processing by GOTHIC.

### 1.5.2 Hill Climbing

Although we have performed Gaussian smoothing prior to the hill climbing, no image is ideal and there are residual non-uniformities

and noise. As a result, the peak found by hill climbing is sensitive to the randomly initialized starting point *i.e.*, different starting points may lead to different peaks. To eliminate such uncertainties, we repeat 1,000 instances of the hill-climbing subroutine initialized at random starting points and enlist all peaks thus found.

Figure 7a and Figure 7b show how one random point ascends up to the peak via hill climbing. In both cases, the initialized point is near the edge of the galaxy envelope and takes small steps until it reaches the peak at one of the nuclei. There were 10 steps taken to reach a peak in the former, and 9 steps in the latter; each step has been marked by a red pixel. Figure 8a and Figure 8b show the peaks (marked in red) obtained by repeating hill climbing process for Reps 2, 3 respectively. Rep 2 (Figure 8a) has peaks scattered across the envelope due to residual non-uniformities in the smoothed image. Although we perform 1,000 hill climbs, not all peaks are stored (only the unique peaks are stored). Next we specify these conditions and provide the pseudocode for the hill climbing sub-routine.

The formal hill climbing algorithm is given in the algorithm HILL-CLIMB. It takes as its argument the randomly initialized starting point  $pt$ .  $reg$  is list  $\{(x, y)\}$  of pixel coordinates that represents the search region for peak finding (for example, the red region in Figure 6a). Finally, the variable  $img$  is a dictionary that maps coordinates  $(x, y)$  of the smoothed image to its corresponding pixel value (between 1 and 255 for grayscale images). NULL represents a dummy value used for initialization.

The procedure GET-NEIGHBORS returns a list of pixels upto the nearest 3<sup>rd</sup> neighbors (in terms of the supremum norm) of the input point  $pt$ . These neighbors form a  $7 \times 7$  box at the centre of which lies the point  $pt$ . Variable  $reg$  is also required by the procedure so that it can exclude any point in the  $7 \times 7$  box that may lie outside the search (red) region.

Semantically, the variable  $newpt$  represents the coordinate that has the highest pixel value in comparison to the current  $pt$ . Its value is determined by lines 4 to 7 by iterative comparison of pixel values with each of the neighbors of  $pt$  using the image dictionary  $img$ . If no higher neighbor is found, we obtain the condition  $pt = newpt$ . This is to be interpreted as — *no higher neighbor of  $pt$  was found, so it must be a peak*. Finally, the while loop exits due to the guard condition in line 2 and it is returned in line 9.

It is possible to consider only the 1<sup>st</sup> or 2<sup>nd</sup> nearest neighbors when performing the neighbor search, however, it leads to a longer trail between the initial point and the final peak due to smaller discrete steps. This results in a slowdown of the HILL-CLIMB procedure. For optimal performance, we consider 3<sup>rd</sup> neighbors only. Using higher-order neighbors such as 4, 5 may lead to false negatives in the scenarios where the DNG peaks are in close proximity *i.e.*, the highest peak would always be chosen if it happens to be a close neighbor of the second highest peak. Hence, it could be mistakenly reported as a single nucleus galaxy.

### 1.5.3 Iterated Hill Climbing

Algorithm 1.5 is the iterated hill climbing algorithm that is used to find the list of candidate peaks. It takes as input the search region  $reg$  and the image dictionary  $img$ . Line 1 initializes the variable  $peak\_list$  to the empty list  $\Phi$  and the counter  $i$  is set to 0 in line 2.

It first chooses a random point in the search region via procedure CHOOSE-RANDOM at line 3, and it is subsequently passed to the hill-climbing subroutine in line 4. After a peak has been found, it is subjected to the following elimination conditions to decide if it should be included in  $peak\_list$

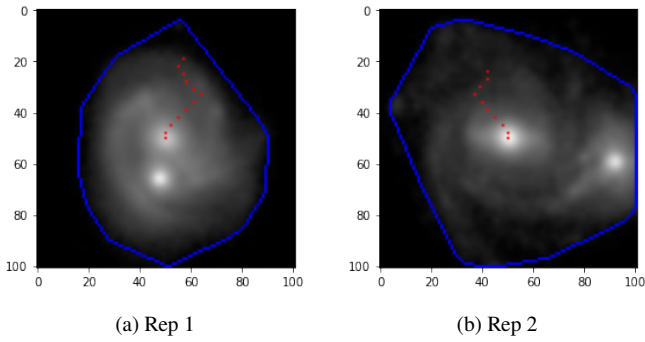


Figure 7. Trace of Hill Climb

- (i) The SNR at the peak must be greater than 3 standard deviations
- (ii) The peak should not already exist in the list of peaks
- (iii) No neighboring pixel (upto the nearest third) must already exist in the list of peaks — This condition has been included because HILL-CLIMB uses neighbors upto the nearest third in finding the highest neighboring pixel. Hence, it does not make sense to have two peaks in the peak list that are atmost third neighbors apart. This scenario is only relevant when any two peaks are equal in pixel value and happen to lie in each others' neighborhoods.

Only if the above three conditions are satisfied is the new peak appended to the list in line 10. Finally, the peak list is returned after 1,000 iterations are concluded. It is precisely this peak list that has been marked in red in Figure 7a and Figure 7b respectively. As mentioned previously, Figure 8a has multiple reported peaks within the galaxy envelope due to non-uniformity. Moreover, Figure 8b has two peaks which clearly belong to two distinct objects and such cases are a potential source of false positives. Next, we present the techniques to handle such cases.

#### 1.5.4 Connected Components

Simply stated, the number of connected components is the number disjoint portions of the search region of a galaxy. For example, there is 1 connected component in Rep 5 (Figure 6a) and 2 connected components in Rep 7 (Figure 6b). The algorithm for computing disjoint regions is a standard one and can be easily found in Cormen et al. (2009).

The astute viewer may point out that Rep 5 (Figure 6a) actually contains 2 connected components and that Rep 7 (Figure 6b) contains 3 connected components. Although it is true, these components are too small in size to represent any astronomical object (star or galaxy) in SDSS. It is an artefact of the noise in the image. Hence, all components that are *smaller* than a certain threshold size are ignored.

#### 1.5.5 Most Probable Component

When there are multiple peaks dispersed across multiple components, it is crucial to identify which component contains our peak(s) of interest. In a nutshell, a component  $C$  is a set of pixel coordinates  $C = \{(x, y)\}$ . The number of pixels in a component would be the cardinality,  $|C|$ . The search region for an image can be typically broken down into  $n$  components as  $\{C_1, C_2, \dots, C_n\}$ . One of these components contains our peak of interest, denote it by  $C_p$ . We describe intuitively the expected characteristics of such a  $C_p$  with the following heuristics.



Figure 8. Peaks for 1000 instances of Hill Climb

**Heuristic (i) :** The component must be close to the centre of the image. This is intuitive as we take a cutout centred at the coordinates of an object.

**Heuristic (ii) :** The component must have a higher cardinality than other components. This ought to be true in most cases as other stray objects on the line of sight of the cutout are expected to be smaller in size.

It would be incorrect to choose a component that has higher cardinality but is distant from the centre of the image as it is more likely to represent a stray object on the line of sight. Hence heuristic (i) above must be given higher priority than heuristic (ii).

To capture these notions into a mathematical formulation, we define the *midpoint* of a component as the average of its constituent pixel coordinates *i.e.*,  $m_C = \left( \frac{\sum x}{|C|}, \frac{\sum y}{|C|} \right)$  for all  $(x, y) \in C$ . We also define the *distance* of component is its 2-D pixel distance from the centre of the image,  $p^2$ . Formally stated, it is  $d_C = \sqrt{\|m_C - p\|^2}$ . Next, we informally describe the steps to identify the most probable component  $C_p$ .

**Step 1** - We aggregate the components into bins of 10 units of pixel distance. For example, all components with their distance  $0 \leq d_C < 10$  would be put in the first bin,  $10 \leq d_C < 20$  would be put in the second bin and so on. After the binning process, we consider only the first bin,  $\mathcal{B}_1$ , as all its constituent components are closest to the centre of the image. This captures heuristic (i).

**Step 2** - We sort the constituents of  $\mathcal{B}_1$  in descending order of their cardinality. Finally, we set the most probable component  $C_p$  as the first element of  $\mathcal{B}_1$ , which would be the largest component. This captures heuristic (ii).

This two step procedure gives more priority to heuristic (i) than (ii) because the binning procedure eliminates components that are far from the centre. The large component from only the *first* bin  $\mathcal{B}_1$  is chosen.

## 1.6 Final Classification

### Representatives Chosen - 2, 3

To provide the final verdict for whether a galaxy is single or double nuclei, we use a simple criteria as follows

**Case 1** - If no peak is found by iterated hill climbing, the source is

<sup>2</sup> The  $40'' \times 40''$  cutouts almost always correspond to 100 pixel  $\times$  100 pixel images. Thus, the centre coordinate  $p = (50, 50)$

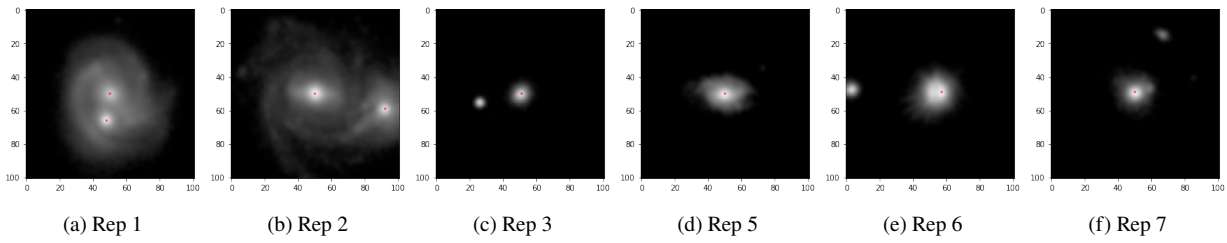


**Figure 9.** Final peaks after classification (marked as red pixel)

discarded.

**Case 2** - If one peak is found, then the galaxy is a single nucleus galaxy.

**Case 3** - If the number of peaks found is  $\geq 2$ , then we have two sub-cases based on how the peaks are distributed in the various *connected-components* of the search region

(i) *Subcase 3.1* - If the two brightest peaks are in the same component, then the galaxy is double nuclei. Otherwise it is judged as a single nucleus.

(ii) *Subcase 3.2* - The connected component with the highest *chance* of representing a bonafide galaxy is selected. If it has one peak only, it is reported as a single nucleus. Otherwise, it is reported as double nuclei.

We justify each case of our classification criteria -

**Case 1** - It is possible that the Iterated Hill Climbing procedure returns no peak. This scenario can occur due to the first elimination criterion mentioned at the end of [Section 1.5.2](#).

**Case 2** - This represents a non ambiguous detection of a single nucleus galaxy.

**Case 3** - The detection of more than one peak requires careful analysis. If two or more peaks are detected, naively adjudging them as double nuclei would lead to excess false positive detections. [Figure 8b](#) is one such case where two peaks are detected, but they clearly belong to two distinct objects in the same field of view, and hence must be adjudged as a single nucleus galaxy. This *intuitive* notion of distinct objects is captured by the *mathematical* notion of connected components ([Section 1.5.4](#)). Moreover, it is not enough to simply report that a galaxy is single/double nuclei. We wish to know the exact coordinates of the peak(s) detected. Thus, in the case where  $\geq 2$  peaks are detected, it must be figured which two of the multiple peaks faithfully represent a double nuclei galaxy. [Figure 8a](#) represents a scenario of multiple peaks in one connected component. In the general scenario, we would have multiple peaks detected in multiple connected components. To faithfully determine whether the galaxy is single/double nuclei, we require a notion of the *most probable* connected component that is likely to contain the peak(s) of interest ([Section 1.5.5](#)).

After the peaks have been located, we transform their pixel coordinates to astronomical coordinates (ra, dec) with the help of *astropy*.

### 1.6.1 Edge Cases in the Classification

We mention the edge cases that *GOTHIC* cannot handle reliably.

(i) If the Canny procedure cannot detect edges, the galaxy is not amenable to further processing and hence rejected.

(ii) We expect that the centre of the cutout would be inside the convex hull formed from the edges reported by Canny. If this is not

the case, the object (if any) at the centre of the image is not bright enough for further processing, and subsequently rejected.

(iii) On rare occasions, *scipy* throws errors while fitting the Sérsic profile to the pixel histogram. In other cases, it can time out as well. Such galaxies are rejected.

### 1.6.2 Performance of *GOTHIC* on the representatives

We show the peaks detected by *GOTHIC* on the representative examples in [Figure 9](#). The final classification reported and peaks reported by *GOTHIC* agree well with the representative images in [Figure 1](#) and their corresponding descriptions in [Table 1](#).

The two nuclei in the bonafide DNG examples (Rep 1 and Rep 2) are clearly identified. Rep 3 and Rep 7 showcase a star/galaxy in the line of sight of the central object respectively, and *GOTHIC* classifies both of them as a single galaxy. Rep 5 is a single nucleus galaxy with no object in its line of sight and is correctly classified as a single nucleus galaxy. Rep 6 is a star (mislabelled as galaxy in SDSS) and although it is reported to have one peak, it does not make a difference to our final aim of searching for DNGs from a blind sample (Main Section 4). Rep 4 is a faint galaxy and *GOTHIC* does not detect any peaks in it, and hence has been rightly excluded from [Figure 9](#).

## 2 PERFORMANCE OF *GOTHIC* ON THE GIMENO CATALOG

The pixel coordinates of the detected peak(s) when *GOTHIC* is run on the Gimeno Catalog and the control sample is shown in [Table 2](#) and [Table 3](#) respectively. Each row in the table contains the `objID` of the galaxy and the pixel coordinates of the detected peaks within the cutout.

## REFERENCES

- Canny J., 1986, [IEEE Transactions on Pattern Analysis and Machine Intelligence](#), PAMI-8, 679
- Caon N., Capaccioli M., D’Onofrio M., 1993, [MNRAS](#), 265, 1013
- Cormen T. H., Leiserson C. E., Rivest R. L., Stein C., 2009, Introduction to Algorithms, Third Edition, 3rd edn. The MIT Press
- Price-Whelan A. M., et al., 2018, [The Astronomical Journal](#), 156, 123
- Sérsic J. L., 1963, Bulletin of the Argentine Association of Astronomy, 6, 41
- Sklansky J., 1982, [Pattern Recognition Letters](#), 1, 79
- Talvila E., Wiersma M., 2012, Simple derivation of basic quadrature formulas ([arXiv:1202.0249](#))
- Vincent O. R., Folorunso O., 2009, in Proceedings of Informing Science & IT Education Conference (InSITE).
- Virtanen P., et al., 2020, [Nature Methods](#), 17, 261

**Table 2.** Results of *GOTHIC* on the Gimeno Catalog - For each objID, the pixel coordinates of the detected peaks is given

objID	Peak 1	Peak 2
1237678661428314227	(50, 50)	(56, 41)
1237651737370296329	(50, 51)	(36, 63)
1237661433243828392	(61, 51)	(50, 50)
1237680265075884063	(62, 32)	(50, 50)
1237678622230773769	(50, 50)	(69, 56)
1237663530798219364	(50, 49)	(38, 37)
1237680332175769723	(49, 50)	(57, 40)
1237661950781685800	(51, 32)	(50, 50)
1237668670253564040	(50, 50)	(45, 39)
1237661850396327969	(50, 50)	(21, 50)
1237680286536826907	(49, 50)	(1, 33)
1237658801497178131	(50, 50)	(43, 42)
1237679436129632275	(50, 50)	(50, 58)
1237661816027938877	(41, 44)	(50, 51)
1237655463774191765	(93, 24)	(50, 49)
1237680529207066652	(50, 50)	(50, 62)
1237665329853562899	(57, 24)	(50, 49)
1237661063879000073	(50, 50)	(69, 69)
1237658204517171275	(50, 50)	(44, 25)
1237679456529743995	(56, 58)	(46, 42)
1237664289930346555	(53, 62)	(50, 48)
1237661950783979531	(50, 50)	(60, 60)
1237680271501426770	(50, 50)	(48, 37)
1237661358620082187	(50, 50)	(57, 57)
1237653612113166459	(50, 50)	(61, 53)
1237651539239895057	(51, 50)	(45, 59)
1237657589780512816	(50, 50)	(43, 42)
1237654400761790563	(50, 50)	(59, 55)
1237650761852846175	(50, 50)	(68, 59)
1237654382516699209	(49, 50)	(49, 36)
1237655472898637896	(50, 50)	(52, 40)
1237670961092558855	(50, 50)	(28, 16)
1237657856073269409	(50, 50)	(59, 27)
1237670961628971177	(50, 61)	(49, 50)
1237666300016591063	(50, 50)	(66, 59)
1237655463772618940	(50, 50)	(34, 55)
1237665569292943466	(50, 50)	(41, 49)
1237661977085018198	(50, 50)	(68, 40)
1237678598094454843	(50, 50)	(49, 45)
1237657771786960904	(45, 59)	(50, 50)
1237664871897038979	(50, 50)	(52, 40)
1237679581622698224	(38, 47)	(49, 49)
1237654640211656710	(33, 92)	(50, 50)
1237680245191868529	(47, 51)	(51, 51)
1237658491207680027	(74, 68)	(48, 51)
1237666301638279613	(50, 50)	(59, 92)
1237667734504407135	(54, 56)	(39, 59)

**Table 3.** Results of *GOTHIC* on the Control Sample - For each objID, the pixel coordinates of the detected peak(s) is given

objID	Peak 1	Peak 2
1237648720142401611	(50, 50)	-
1237650795146510627	(50, 50)	-
1237650795146445031	(50, 50)	-
1237648720142401670	(50, 50)	-
1237648720142532891	(50, 50)	-
1237650795146510903	(30, 37)	-
1237648720142401774	(40, 10)	-
1237650795146576091	(50, 50)	-
1237650795146641532	(50, 50)	-
1237650795146576030	(50, 50)	-
1237650795146444862	(9, 37)	-
1237650795146575935	(28, 68)	-
1237651800158896649	(60, 50)	(45, 50)
1237650794609574093	(50, 50)	-
1237648720679469274	(50, 50)	-
1237648721216274697	(50, 50)	-
1237650795683512507	(50, 50)	(40, 61)
1237650795683578031	(50, 48)	(52, 53)
1237648721216340148	(50, 50)	-
1237650795683578073	(4, 45)	-
1237648721216405657	(50, 50)	(52, 36)
1237648721216274720	(41, 28)	-
1237650795683446969	(9, 1)	-
1237650796220514489	(50, 50)	(42, 45)
1237650795683512955	(50, 50)	-
1237650795683512690	(50, 50)	-
1237648720142336237	(50, 50)	-
1237651799621959987	(50, 50)	-
1237651799621894422	(54, 50)	(55, 55)
1237650795146379400	(50, 50)	-
1237648720142270656	(50, 50)	-
1237650794609442930	(50, 50)	-
1237648720142336185	(50, 50)	-
1237650795683512717	(19, 17)	-
1237650795146379447	(50, 50)	-
1237651799621959813	(64, 50)	(50, 50)
1237650795146379491	(50, 50)	-
1237650795683446896	(50, 50)	-
1237650795683446947	(50, 50)	-
1237650795683447026	(6, 10)	-
1237648720679338392	(51, 50)	-
1237648720679338241	(50, 50)	-
1237648720679338261	(15, 14)	-
1237648720679338252	(50, 50)	-
1237648721216209095	(50, 50)	-
1237650795683446889	(24, 48)	-
1237650796220252232	(50, 50)	-